



FACULTAD DE CIENCIAS

SECCIÓN DE FÍSICA

END OF DEGREE PROJECT

**3D-LASER NANOLITHOGRAPHY IN YAG:  
MEASUREMENT OF REFRACTIVE INDEX  
CHANGES AND DESIGN OF A PHOTONIC  
CRYSTAL WAVEGUIDE**

Supervised by  
**Airán Ródenas Seguí**

Realized by  
**Marcos Esquivel González**

July 2022

# Abstract

---

In the present work, a study of photonic structures is carried out simultaneously from an experimental and computational point of view. Experimentally, the yttrium aluminium garnet (YAG) optical crystal has been used to study the wet-chemical etching enhancement in sub-micron width line tracks written with the 3D laser writing (3DLW) technique. This technique uses a femtosecond pulse laser ( $\sim 150$  fs) in the NIR spectral range ( $\sim 800$  nm). The size of the hollow pores obtained by the wet-etching in lithographed areas, with widths of sub-micron size and lengths in the sub-mm order, are ideal for the creation of photonic structures. In this context, it has been possible to analyse and identify the laser configurations that achieve a higher etching rate in this crystal depending on scan speed, laser pulse repetition rate, and pulse energy. Also, the possibility of creating air pores of different diameters or with a circular shape can be controlled by changing the energy pulses of the laser. On the other hand, by means of a wavefront phase imaging (WFPI) technique developed at Woptix S.L., the order of the refractive index change ( $10^{-2}$ ) produced at sub-micron scale in YAG due to the 3DLW process has been characterized for the first time. Complementarily, a numerical study of a 2D nanopore hexagonal photonic lattice in YAG has been performed by means of commercial software (BandSOLVE, RSoft). Thus, this allows to identify the configuration with an optimal photonic bandgap, found to be for light propagating with its electric field lying within the plane. Finally, possible confined modes for a microstructured optical waveguide (MOW), simply designed with a cladding hexagonal structure and a single pore defect in the centre as core, have also been investigated.

# Resumen

---

En el presente trabajo se realiza un estudio tanto experimental como computacional de estructuras fotónicas. En el ámbito experimental, se estudia la mejora en el grabado químico húmedo producida en cristal óptico de granate de itrio y aluminio (YAG) para líneas trazadas con grosor sub-micrométrico mediante la técnica de escritura láser 3D (3DLW). Esta técnica utiliza un láser de pulsos de femtosegundos ( $\sim 150$  fs) con longitudes de onda en el rango NIR ( $\sim 800$  nm). El tamaño de los poros vacíos obtenidos por el grabado húmedo en zonas litografiadas, con anchuras de tamaño sub-micrométrico y longitudes inferiores al milímetro, son ideales para la creación de estructuras fotónicas. En este contexto, se ha podido analizar e identificar las configuraciones láser que consiguen una mayor tasa de grabado en YAG en función de la velocidad de barrido, la tasa de repetición de los pulsos láser y la energía de los pulsos. Asimismo, la posibilidad de crear poros de aire a diferentes diámetros o con forma circular se ha podido controlar cambiando la energía de pulso del láser. Por otro lado, gracias a una técnica de medición de frente de onda (WFPI) desarrollada en Wootix S.L., se ha podido caracterizar por primera vez el orden del cambio de índice de refracción ( $10^{-2}$ ) producido a escala sub-micrométrica en YAG debido al proceso 3DLW. Complementariamente, se ha realizado un análisis numérico de una red fotónica hexagonal de nanoporos 2D en YAG mediante software comercial (BandSOLVE, RSoft). De esta manera, se consigue identificar la configuración con un *bandgap* fotónico (PBG) óptimo, encontrado para la luz que se propaga con su campo eléctrico dentro del plano. Finalmente, se han investigado los posibles modos confinados para una guía de onda microestructurada MOW, simplemente diseñada con una estructura hexagonal de revestimiento y un único defecto de poro en el centro como núcleo.

# List of abbreviations

---

<b>3DLW</b>	3D laser writing
<b>BSE</b>	Backscattered electrons
<b>FCC</b>	Face centered cubic
<b>FF</b>	Filling factor
<b>FWHM</b>	Full width at half maximum
<b>HW</b>	Half wave plate
<b>IBZ</b>	Irreducible Brillouin zone
<b>MIR</b>	Mid-infrared
<b>MOW</b>	Microstructured optical waveguide
<b>NA</b>	Numerical aperture
<b>NIR</b>	Near-infrared
<b>OPD</b>	Optical path difference
<b>PBG</b>	Photonic bandgap
<b>PCF</b>	Photonic crystal fiber
<b>PP</b>	Pulse picker
<b>SE</b>	Secondary electrons
<b>SEM</b>	Scanning electron microscopy
<b>SIF</b>	Step index fiber
<b>Ti:Sa</b>	Titanium Sapphire oscillator
<b>UV</b>	Ultraviolet
<b>VIS</b>	Visible
<b>WFPI</b>	Wave front phase imaging
<b>YAG</b>	Yttrium aluminium garnet



# Contents

---

<b>1</b>	<b>Introduction</b>	<b>1</b>
<b>2</b>	<b>Methodology</b>	<b>3</b>
2.1	Pores fabrication . . . . .	3
2.1.1	Femtosecond Pulses Laser writing . . . . .	3
2.1.2	Polishing and wet chemical etching . . . . .	5
2.1.3	Optical microscope and SEM measurements . . . . .	6
2.2	Wave Front Phase Imaging(WFPI) . . . . .	8
2.3	Simulations with RSoft: BandSOLVE . . . . .	10
2.3.1	Photonic Lattice: Concepts . . . . .	11
2.3.2	Band structure and functioning of BandSOLVE . . . . .	12
2.3.3	Hexagonal lattice with BandSOLVE . . . . .	14
<b>3</b>	<b>Results discussion</b>	<b>16</b>
3.1	Pore Characterization . . . . .	16
3.1.1	Pore length study at equal etching time . . . . .	16
3.1.2	Pore width and height analysis. . . . .	19
3.2	Refractive index in lithographed zoned . . . . .	21
3.3	Pore Hexagonal lattice: Band structures and wave guides . . . . .	24
3.3.1	2D model: Bandgaps . . . . .	24
3.3.2	3D model: bandgaps in longitudinal direction . . . . .	27
3.3.3	Analysis of a Microstructured Optical Waveguide . . . . .	29
3.3.4	Fabrication of an hexagonal lattice . . . . .	34
<b>4</b>	<b>Conclusions</b>	<b>36</b>
<b>5</b>	<b>References</b>	<b>38</b>
	<b>Appendix</b>	<b>I</b>
A	Cross-sectional pore measurements . . . . .	I
B	Error propagation . . . . .	II

# List of Figures

---

2.1	Distribution of the spectral width of Titanium Sapphire oscillator (Ti:Sa)(a) and output power of pulse picker (PP) as a function of the relative angle with half wave plate (HW)(b). . . . .	4
2.2	Elements of the laser setup. . . . .	5
2.3	YAG sample polished on the topside to expose the vertical lines (already etched) and the polisher. . . . .	6
2.4	Microscopes used and gold coating for scanning electron microscopy (SEM)	7
2.5	Methodology followed to measure height and width of pores. . . . .	8
2.6	Photograph of wave front phase imaging (WFPI) device and schematic diagram of operation. . . . .	9
2.7	Reciprocal and real lattice concepts. . . . .	12
2.8	Lattice, Bloch wave vector in real and reciprocal space, and the resulting band structure. . . . .	13
2.9	Propagation modes for a longitudinally extended hexagonal lattice of pores.	14
2.10	Pore lattice forming a hexagonal structure. . . . .	15
3.1	Pores 41h wet-etched with 1k20 set in YAG. . . . .	17
3.2	Forward traces for 41h wet-etching pores as a function of writing velocities	18
3.3	Backward traces for 41h wet-etching pores as a function of writing velocities	18
3.4	scanning electron microscopy (SEM) images for the transversal plane of pores varying energy pulses every four pores . . . . .	20
3.5	Minimum size limits achieved for the wet-etched nanopores. . . . .	21
3.6	Raman photography of the written plane in the XZ view. . . . .	21
3.7	Intensity images used for OPD reconstruction and the resulting OPD map.	22
3.8	OPD profile along X-axis . . . . .	23
3.9	Real and reciprocal space domains of the hexagonal lattice for lattice parameter $1\mu m$ and pore diameter $0.375\mu m$ . . . . .	24
3.10	Gap map and width of the first band gap for TE and TM modes as a function of pore diameter. . . . .	26
3.11	Bandgap width of TM modes as a function of diameter for different spectral ranges. . . . .	26
3.12	Band structure for the pore diameter with the highest bandgap in the different YAG spectral ranges . . . . .	27

3.13	New path followed in the scanning of wave vectors to elaborate the band structure. . . . .	28
3.14	Band diagram using two different k-paths. . . . .	28
3.15	First periodic domain of integration considered. . . . .	30
3.16	Spatial distribution of the squared magnetic intensity for each mode. . .	31
3.17	Second integration domain considered. . . . .	32
3.18	Modes traversing the vector $\mathbf{K}$ in longitudinal direction from $(0, 1, 0)$ to $(0, 30, 0)$ [ $\mu m^{-1}$ ]. . . . .	33
3.19	V number as a function of $k_y$ . . . . .	34
3.20	Hexagonal lattice made by 3DLW . . . . .	35

## List of Tables

---

3.1	Different combination sets done with 3DLW technique. . . . .	16
3.2	Cross-sectional measurements of pores. . . . .	20
3.3	Frequencies and effective indices values of the first 8 modes for Bloch wave vector $\mathbf{K} = (0, 10, 0)[\mu m^{-1}]$ . . . . .	30
3.4	Frequencies and efective indices for the first eight modes considering second domain of integration. . . . .	33
A.1	All cross-sectional measurements of pores. . . . .	I

# 1. Introduction

---

## *Resumen*

---

En este apartado se realiza una introducción que enmarca la importancia que están suponiendo las estructuras fotónicas en el campo del guiado de luz, haciendo una breve revisión del estado del arte en esta materia. Seguidamente, se describe el proceso que ha llevado a la microestructuración de cristales ópticos a usar láseres de femtosegundos y así introducir la técnica de escritura láser 3D (3DLW) usada en este trabajo. Finalmente, se presentan las diferentes partes en las que se estructura este trabajo. Estas, principalmente, han sido la caracterización del cambio de índice de refracción en zona litografiada con láser, el estudio del aumento de la tasa de grabado en zonas escritas con láser mediante la técnica 3DLW, así como estudios numéricos de bandgaps fotónicos y de una guía de onda microestructurada posibles de fabricar en laboratorio.

---

Photonic applications of the nanostructuring of dielectric optical crystals have been a breakthrough in the field of light guidance. One example is non-linear photonic crystals (NPCs), such as  $\text{LiNbO}_3$ , that can be used to achieve spatial reconfiguration of a light beam at a new frequency<sup>1</sup>. Additionally, the most exciting challenge lies in photonic integrated circuit (PIC) technology<sup>2</sup>, which enables interesting applications such as in the field of data science or quantum information. To achieve this, the importance of realising low-loss optical waveguides (MOW) with small radii and high structuring efficiency is claimed, where femtosecond lasers are providing great utility<sup>3,4</sup>. In this context, another notable example of the potential of 3D nanostructuring of optical materials comes from the field of optical fibres, where single-mode photonic crystal fiber (PCF) have provided superior functionalities than ordinary unstructured glass.

Therefore, the correct microstructuring of optical crystals is of crucial importance. At first, the optical modification of crystals by ultraviolet radiation (UV modification) was widely known<sup>5</sup>. In this case, ionisation occurs in the material by modifying the electronic bonds of its atoms and thus producing changes in the refractive index in that area. However, this is a problem for nano-structuring purposes (photonic crystals), as a single UV photon is able to structurally change the crystal before reaching the focus point, so that it is very difficult to sculpt the medium in its volume. Thankfully, the phenomenon of multi-photon absorption and tunnel effects<sup>6</sup> can avoid this problem and achieve alteration in-volume photo-modifications. For this purpose, the use of femtosecond lasers in the  $1\ \mu\text{m}$  near-IR range has demonstrated this capability by achieving 3D stress-induced nanomodifications within the material<sup>7</sup>, which provokes changes in the refractive index. This technique is known as 3D laser writing (3DLW).

Although there are already articles characterising the refractive index change produced by 3DLW in glasses and crystals<sup>8</sup>, the case of 3D nanolithography in crystals, where a high-NA objective (1.4 NA) is used and sub-micrometric traces are produced, has never been investigated before. In this work, thanks to the use of a wave front phase imaging (WFPI) technique, a first value of the refractive index change in YAG

crystal is calculated. Also, it has been seen the change in chemical reactivity produced by 3DLW nanolithography<sup>9</sup>. The knowledge of these processes allows for the creation of centimetre-long air pores and hundreds of nanometres thick, ideal for the fabrication of air-pore lattices in YAG as photonic nanodevices. Finally, some of the possible structures that can be achieved in YAG with this technique are studied by means of BandSOLVE, in order to characterise optimum photonic structures for near-future development.

## 2. Methodology

---

### *Resumen*

---

En este capítulo se explicará el proceso llevado a cabo para la creación de nanoporos de grosor sub-micrométrico en YAG, haciendo un grabado químico en líneas nanoescritas con la técnica 3DLW. Además, se presentará la técnica de medición de la fase del frente de onda, WFPI, para el cálculo del cambio de índice de refracción en la zona nanolitografiada con láser. Por último, se detallarán conceptos de los cristales fotónicos y se explicará el funcionamiento de BandSOLVE para simulaciones numéricas de estructuras fotónicas.

---

This chapter will explain the methods used for the nanofabrication of air pores in YAG, the measurement of the wavefront phase for characterising the index refraction changes, and the BandSOLVE software, used for studying photonic structures with numerical simulations.

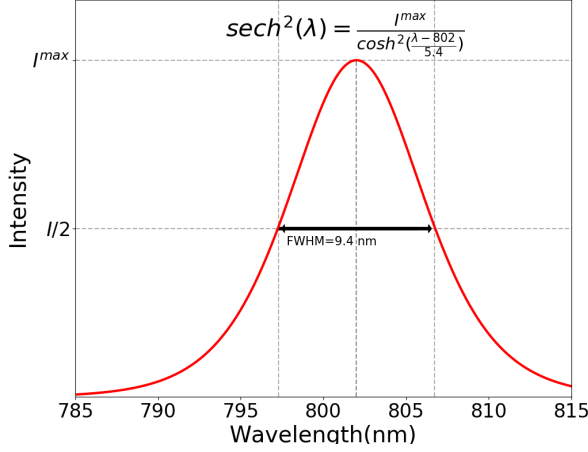
### 2.1. Pores fabrication

The material used for pore creation is YAG crystal. Within an XY plane in the crystal, sample is written with sub-micron width straight lines using 3DLW technique with a femtosecond pulse laser. The lithographed zone is then surfaced by polishing until it reaches one of the ends of the lines. Finally, wet chemical etching is carried out with a solution that attacks the lithographed area much more preferentially to form the air nanopores within the written lines. This whole process is developed in the following subsections.

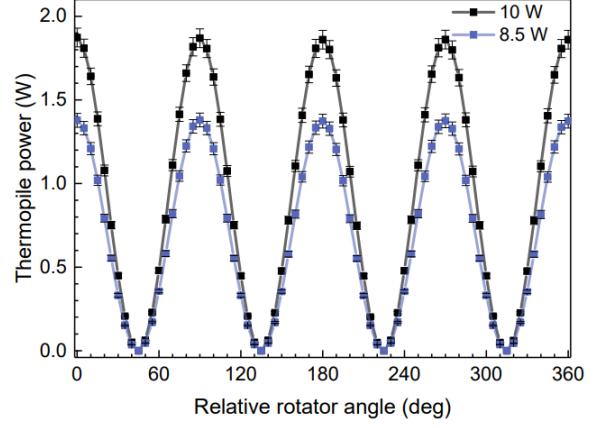
#### 2.1.1 Femtosecond Pulses Laser writing

The structure alteration in YAG is created and controlled thanks to a really short pulse laser. Exactly, the setup performance with femtoseconds pulse in the NIR range, and with high frequency of pulses (kHz-MHz order). With this configuration 3DLW is possible thanks to multi-photons absorption in the focus point. This phenomenon causes changes in the electronic bonds in that area without breaking them, resulting in small changes in the density and refractive index of the lithographed area, useful for wet etching of air pores.

On the other hand, if the power radiated to the material is too high, it can cause microcracks in the focused spot, i.e., the complete breaking of the crystal bonds. These microcracks can propagate along the crystal, making the situation worse. Furthermore, at high power the crystal can even melt at the focal points because it does not have time to cool down between energy pulses. To avoid all these problems, it is necessary



(a) FWHM is 9.4 nm and Pearson coefficient  $R^2 \simeq 0.99$ .



Source: Melián and Seguí<sup>12</sup>

(b) Power of the PP is measured with a Thermopile. Black curve is the interesting curve as it corresponds to 10 W pumping power.

**Figure 2.1:** Distribution of the spectral width of Ti:Sa(a) and output power of PP as a function of the relative angle with HW(b).

to control the frequency and energy of the pulse in the pulsed laser. The main elements used for the operation of the laser are explained in the following.

Regarding the functioning, for powering the laser in first instance, continuous wave 10 W pumping power is emitted at 532 nm thanks to Millennia eV laser<sup>10</sup>. This pump is sent to Tsunami's ultra-fast Titanium Sapphire oscillator (Ti:Sa)<sup>11</sup> in mode-locking configuration, which produces ultrashort pulses of around  $\simeq 120$  fs, by means of mode-locking, with a high repetition rate (80MHz). This train pulse has an average power of 2W and is typically centred on  $\simeq 802$  nm. The spectral distribution associated can be fitted to a hyperbolic secant distribution with full width at half maximum (FWHM) of  $\simeq 9.4$  nm, this distribution is presented in figure 2.1a. These parameters however, can change significantly, and effective photo-modification can be achieved within a large range of laser wavelengths, pulse durations, repetition rates, and pulse energies.

By construction, linearly polarised light is formed at the output of the Ti:Sa. To control the energy of the pulses within the 3DLW setup, a half wave plate (HW)( $\lambda/2$ ) is placed, which will rotate the polarisation axis of the light. The next element, the pulse picker (PP), will output only the vertical polarisation component of the light, so depending on the angle of the HW with the vertical axis the output power will vary as can be seen in figure 2.1b. The PP is used also to reduce laser pulse repetitions to the working order of kHz-MHz. In addition, if the objective is to create circular pores and decouple the scanning direction, it has been shown that circular polarization may be the most appropriate approach<sup>9</sup>. Therefore, it is also possible to add a quarter lambda plate to the PP output to switch from linear to circular polarization. Next, a Beam Expander(BE) is added to enlarge the width of the free-space laser beam, and adjust it to fill the entrance of the focusing objective(L), as that ensures that the highest NA is achieved(1.4 NA).

Now, to make and move the laser writing site on the sample, there is a high resolution

nanopositioning XY stage on which the sample to be written is fixed. To move the plate in the three dimensions, the Aerotech A3200 software is used to do this work manually or program these movements. The step resolution of the plate is of around 1 nm with maximum speeds of 10 mm/s. All the elements described are showed in figure 2.2 together with others not mentioned.

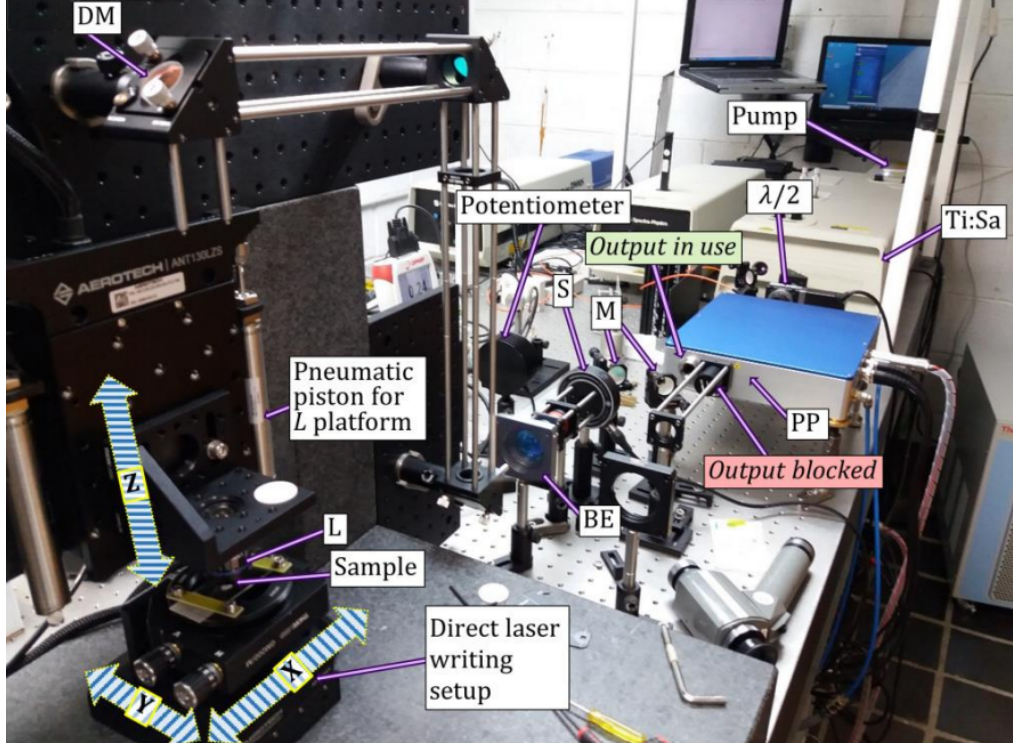


**Figure 2.2:** Elements of the laser setup.

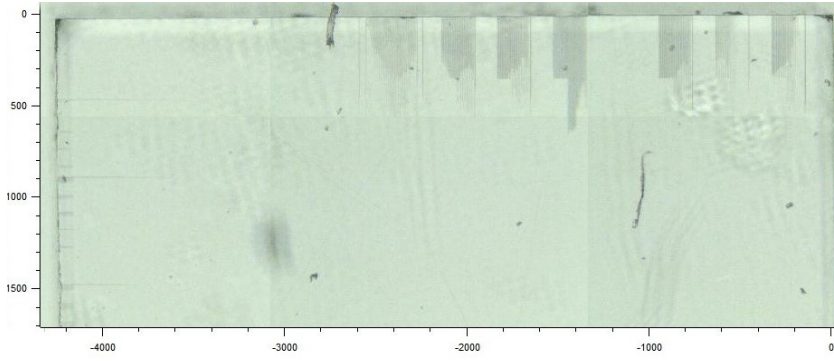
### 2.1.2 Polishing and wet chemical etching

To expose the 3D laser lithographed region to the surface to be wet-chemically etched, and as straight parallel lines were written (figure 2.3a), it was sufficient to polish one side of the crystal up to the edges of the lines.

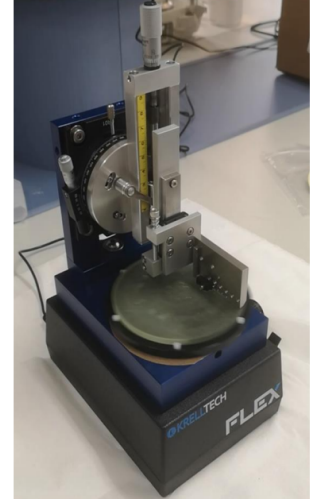
In this process, the sample is first removed from the container used to hold it in the laser, as it was glued with enamel. For this purpose, the crystal is ultrasounded for half a minute in an acetone bath. Once peeled off, the YAG is put back into the ultrasound for 3 minutes to finish removing the enamel remains. Then, the sample is dried with optical paper and taken to the polisher. In the polisher, the crystal is fixed with screws, trying to make it as horizontal as possible with the help of a reference metal. Diamond pads of different roughness are then used to polish the sample by moving them in a circular motion with a motor. The roughnesses available are 30, 15, 9, 6, 3 and 1 micron. They will be used from more to less rough, all with a thin layer of water on top to smooth the polishing. The rougher they are, the less flat they leave the surface but the more size they polish in a given time.

The next step is to create the air pores in the zone written with laser. Phosphoric acid is used for this purpose in a wet etching process. The reason is that this acid has shown





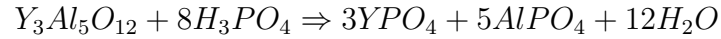
(a) Optical microscope image with axes on micrometer scale. Air pores on the top edge of the crystal in the image.



(b) Polisher

**Figure 2.3:** YAG sample polished on the topside to expose the vertical lines (already etched) and the polisher.

an etching enhancement of five orders of magnitude within nanopores in the lithographed volume<sup>9</sup>. Exactly, the dissolution is carried out by mixing phosphoric acid and water in a volume ratio of 35-65. A magnetic stirrer is also introduced to the sample and then the mix is heated to 75 degrees although it can also be done at room temperature. It is left to act for as long as necessary. The exact chemical process produced in the YAG is not yet confirmed, but Ródenas et al.<sup>9</sup> has published the expected reaction to be:



where  $H_2O$  is generated, so that the reaction products are still in water solution.

In addition to the cross-sectional shape of the pores, as will be studied in this article, the etching rate also depends on the frequency and energy of the pulses used in laser writing. In any case, for certain configurations of energy and pulse, etch rate of lithographed zone can reach  $\sim 100 \mu m/h$  compared to  $\sim 0.5 nm/h$  of unaltered YAG. It is therefore necessary to leave the sample etched for hours if we want air pores of hundreds of microns length. At the same time, it is important to note that a longer etching time will also result in wider pores (although at a slow growth rate).

### 2.1.3 Optical microscope and SEM measurements

Once the air pores have been fabricated, their dimensional measurements will be carried out using microscopes. The length of the nanopores can be achieved using an optical microscope. However, for cross-sectional plane, as sub-microns diameter sizes are achieved, a scanning electron microscopy (SEM) is required.

The optical microscope is a Raman microscope used in transmission (illuminated behind the sample) and has different objectives, which are employed to analyse the pores at different magnifications. The 5x Leica objective has a wide vision field, useful to see several pores in the same shot. On the other hand, for length measurement it

is better to use the Leica 50x lens which, despite having a smaller field of view, has a higher resolution ( $0.6\mu\text{m}$  spatial resolution using Airy criterium<sup>13</sup>).

The width and height of the pores are in the order of hundreds of microns. Therefore, it is necessary to use a scanning electron microscopy. The SEM employed is located in SEGAI, a research support organism of Universidad de La Laguna. In SEM is used an electron beam to acquire information about the sample. There are two electron sources observed in two different detectors<sup>14</sup>:

- Secondary electrons (SE): These are electrons released from the sample due to ionisation caused by the beam. SE imaging gives detailed surface information.
- Backscattered electrons (BSE): Corresponds to the electrons in the beam that have been reflected back due to elastic interactions with the sample. It can give information on deeper levels of the sample as well as the composition of this.

To cross-sectional characterisation is therefore relevant the SE. Also, as YAG is a dielectric material, it is necessary a previous gold sputter coating to make a conductor surface on the sample surface to avoid electron accumulations during SEM observations. Figure 2.4 shows the coating chamber used, as well as the optical and electron microscopes.

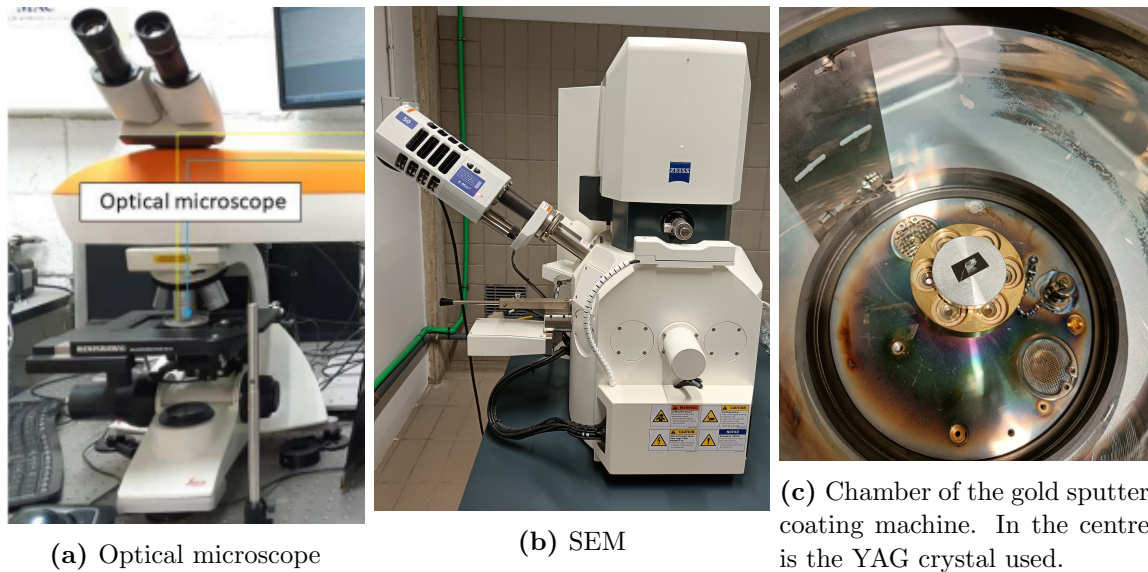


**Figure 2.4:** Microscopes used and gold coating for SEM

Now, for the correct measurement of the images taken from the microscopes, the FIJI ImageJ software is used. This software allows to set the scale of the images and thus measure distances. For the length of the pores, the process is not more detailed. However, for the measurements of the pore cross-sections it is also necessary to apply a light threshold to get the correct pore profile. Figure 2.5 shows a screenshot of the process followed for the cross-sectional dimensions of the pore images taken with SEM.

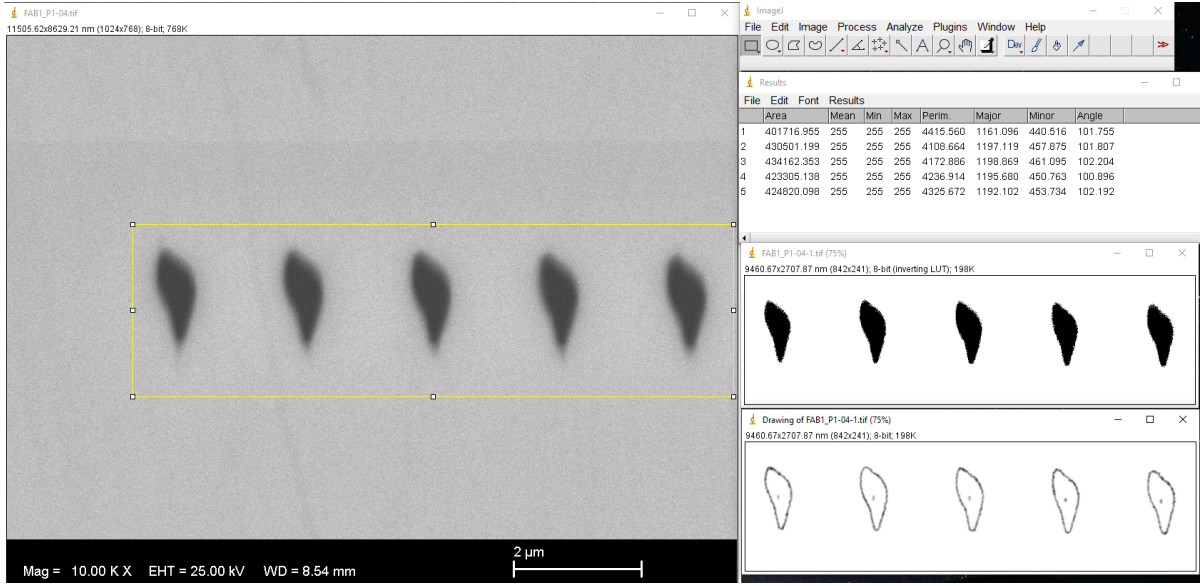


**Figure 2.5:** Methodology followed to measure height and width of pores.

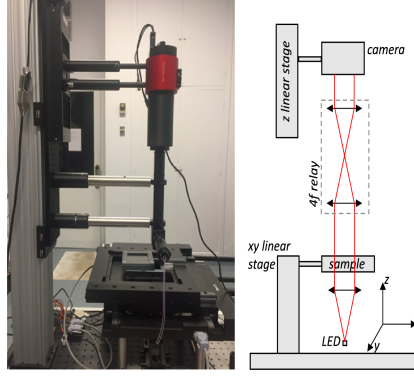
## 2.2. Wave Front Phase Imaging(WFPI)

In order to characterise the change of the refractive index in the 3DLW zone, a partnership has been established with *Wooptix*, a company specialised in wavefront measurement. The technique used, called WFPI, allows optical path difference (OPD) measurements at very high resolution. Specifically, the system used has a lateral resolution of the wavefront of about  $370\mu m$  and height resolution of around  $5 nm$ . This experiment is also interesting to test the resolution of the device by *Wooptix*.

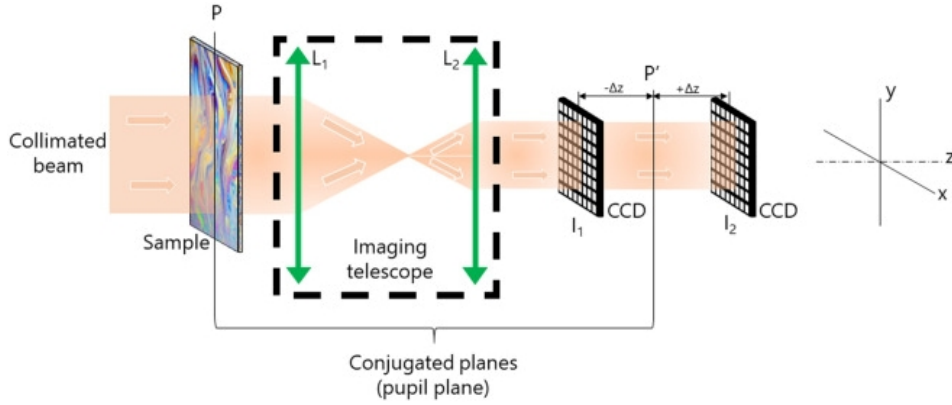
The WFPI works as follows<sup>15</sup>. The crystal sample (YAG) is illuminated with collimated light from a LED (470 nm wavelength), which will give an initial flat wavefront. As the light passes through the sample, due to differences in the refractive index ( $n$ ) in the YAG, it will cause variations in the geometry of the wavefront, which will no longer be flat. In order to introduce this irregular wavefront into the camera, it is previously passed through a 4f relay system. The 4f relay consists of two lenses that will cause a magnification in the optical system according to the focal lengths of the two lenses used. This will enlarge or reduce the size of the wavefront in order to match the capture system size. Once through the 4f relay, 2 intensity images are obtained in planes equidistant to a conjugate plane of the optical system. For clarification purposes, a picture of the instrument together with its conceptual scheme is presented in figure 2.6.

Assuming that the light used is purely monochromatic and moving along the z-axis in a medium with refractive index  $n$ , the light fulfills the plane wave equation. The electric component of light (and equivalent for the magnetic component), with free-space wave number  $k_0$  and angular frequency  $w$ , has the following expression:

$$\begin{aligned}
 E(z, n, t) &= E_0 e^{i\varphi(z, n, t)}, \\
 \varphi(z, n, t) &= k_0 n z + w t + \varphi_0, \quad (k = k_0 n)
 \end{aligned}
 \tag{2.1}$$



Source: Trujillo-Sevilla et al.<sup>15</sup>



Source: Bonaque-González et al.<sup>16</sup>

**Figure 2.6:** Photograph of WFPI device and schematic diagram of operation.

where  $\varphi$  is the phase,  $E_0$  is the amplitude, and  $\varphi_0$  is the initial phase, which can be chosen arbitrarily in practice.

In this way, the device measures the XY phase plane from the intensities measured in the two CCD sensors. To explain how this phase plane is specifically obtained, the following functions must be defined.

Let  $H(x, y)$  be a continuous function defined on the first quadrant of the XY-plane and let  $\mathcal{V}_\alpha$  be a transformation function acting on  $H$  as follows:

$$\mathcal{V}_\alpha\{H\}(x, y) = \int_0^x H(x', \tan(\alpha)x' + y) dx'$$

with  $\alpha \in [-\pi/2, \pi/2]$  and  $x, y > 0$ . Hence, the transformation function  $\mathcal{V}_\alpha$  consists of an integral along a straight line of slope  $\tan(\alpha)$  and ordinate at the origin  $y$ .

Let  $f(x)$  and  $g(x)$  be two functions only defined for positive  $x$  and where  $f(x), g(x) > 0$ . Then,  $D[f, g]$  is defined as:

$$D[f, g](x, y) = \operatorname{argmin}_x(f(x') - y) - \operatorname{argmin}_x(g(x') - y)$$

where  $\operatorname{argmin}_x()$  corresponds to the value on the x-axis within the interval  $[0, x]$  where the function passed as an argument takes the value closest to zero. Therefore, the functional  $D$  is equivalent to the distance on the x-axis of the functions  $f(x)$  and  $g(x)$  when both take the value  $y$ .

Once these functions are presented, the spatial derivatives of the phase are obtained from the intensities  $I_1(x, y), I_2(x, y)$  measured on the two CCDs through the following expressions:

$$\begin{aligned}\varphi_x(x, y) &= \frac{k s^2}{2 \Delta z} \int_{\alpha=-\pi/2}^{\alpha=\pi/2} \cos(\alpha) D[\mathcal{V}_\alpha\{I_1\}, \mathcal{V}_\alpha\{I_2\}] d\alpha \\ \varphi_y(x, y) &= \frac{k s^2}{2 \Delta z} \int_{\alpha=-\pi/2}^{\alpha=\pi/2} \sin(\alpha) D[\mathcal{V}_\alpha\{I_1\}, \mathcal{V}_\alpha\{I_2\}] d\alpha\end{aligned}\tag{2.2}$$

where  $s$  is the size of the pixels in the CCDs,  $k$  is the wavenumber of the light used and  $2 \Delta z$  is the distance between the two detectors. Finally, a numerical integration is performed to recover the phase map  $\varphi(x, y)$  from its derivatives  $\varphi_x$  and  $\varphi_y$ . From the equation 2.1, it can be seen that the phase is expressed in radians. To express the results in metres it would be sufficient to divide by the wave number, obtaining  $\varphi^m$ , which corresponds with the optical path.

The resultant OPD map that finally gives the instrument is calculated now as the difference between an optical path at a point  $(x, y)$  and a point set to correspond to the established path in the crystal  $(x_0, y_0)$ :

$$OPD(x, y) = \varphi^m(x, y) - \varphi_0^m(x_0, y_0)$$

To develop this formula, let assume both optical paths has equal distance travelled  $(z + \Delta z)$ . However, one of them ( $\varphi^m$ ) see a refractive index change  $\Delta n$  in the region of thickness  $\Delta z$ . Therefore, the OPD, basing on equation 2.1, can be expressed as:

$$OPD = \varphi^m(x, y) - \varphi_0^m = [n z + (n + \Delta n) \Delta z] - [n(z + \Delta z)] = (\Delta n) \Delta z$$

In this way, the OPD can be related to the index change that see  $\varphi^m$  respect to the stipulated path  $\varphi_0^m$ .

Moreover, to characterise the index change in the YAG crystal, in addition to knowing the thickness  $z$  of the lithographed zone, it will be necessary to make the optical path difference at the desired positions in the XY plane, for reasons that will be explained in the discussion. For this purpose, it is necessary to subtract the two desired values on the OPD map:

$$\Delta n = \frac{OPD(x_2, y_2) - OPD(x_1, y_1)}{\Delta z} = \frac{OPD_{3DLW}}{\Delta z}\tag{2.3}$$

So this will be the final equation used to characterise refraction index changes in our sample.

## 2.3. Simulations with RSoft: BandSOLVE

BandSOLVE is a simulation tool within RSoft CAD software. With RSoft CAD it is possible to create specific lattice with the refractive index distribution desired. Then, the role of BandSOLVE is to resolve the light waves that can travel through the lattice.



Specifically, the material simulated with RSoft CAD is YAG crystal with air nanopores creating the lattice. The refractive index of YAG was obtained from bibliography<sup>17</sup> and refractive index of air was considered equal to 1. Also, it is important to mention the strong relation between dielectric constant( $\epsilon$ ) and refractive index( $n$ ):

$$n = \sqrt{\epsilon}$$

it is therefore indifferent to talk about refractive index distribution or dielectric constant distribution.

Firstly, the concepts related to this type of lattice, called photonic crystals, are introduced and then, the functioning of BandSOLVE is explained.

### 2.3.1 Photonic Lattice: Concepts

Just as the building blocks of a normal crystal are the atoms, equivalently, in a photonic crystal this role is taken by the dielectric constant<sup>18</sup>. Thus, the real space of a photonic crystal corresponds to the distribution of the dielectric constant within the photonic material, arranged in a periodic order to form a lattice. In this way, the position of the points of the photonic lattice will be given by the primitive lattice vectors( $\vec{t}_i$ ) considered of the real space. Another important concept, the primitive cell, is formed by the primitive vectors on its edges and is defined as the minimum lattice portion that, iteratively repeated in space, forms the whole lattice. By construction, the primitive cell will have a total of one lattice point inside it. The distance between primitive cells is defined with the lattice parameter ‘a’, so it corresponds to the module of the primitive lattice vectors. This lattice parameter doesn’t have to be the same for all  $\vec{t}_i$ ’s. However, in the face centered cubic (FCC) lattice, the one studied in this work, it is.

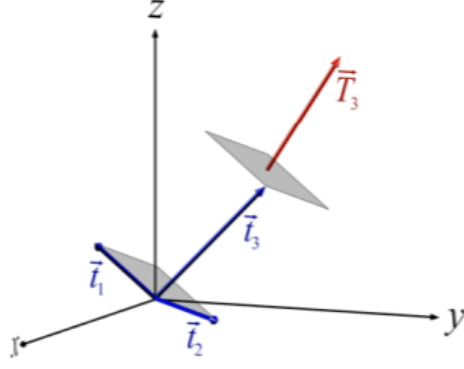
On the other hand, the reciprocal lattice refers to the periodic properties of the lattice in real space and can be interpreted as the field of action of the wave vectors. In this way, the lattice vectors of the reciprocal lattice( $\vec{T}_j$ ) are defined as  $2\pi$  divided by the distance between contiguous and parallel planes of the real lattice(derived from the main equation 2.4). Furthermore, the primitive cell of the reciprocal lattice is called the first Brillouin zone. Due to the periodicity of the material, all possible frequencies of the wave vectors within the lattice are collected in the domain of the first Brillouin zone. Moreover, if additional spatial symmetries of the lattice exist, the first Brillouin zone can be reduced to its most compact form in the so-called irreducible Brillouin zone (IBZ).

$$\vec{t}_i \cdot \vec{T}_j = 2\pi\delta_{ij} \quad \forall i, j \in [1, \text{dimension}] \quad (2.4)$$

Figure 2.7 shows an example of lattice vectors in a FCC lattice(2.7a). Additionally, an schematic construction of one of the three vectors of the reciprocal lattice(2.7b) is presented. From the equation 2.4, for a 3D space, its expression in this case is

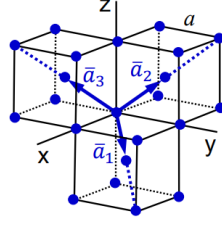
$$\vec{T}_3 = 2\pi \frac{\vec{t}_1 \times \vec{t}_2}{\vec{t}_1 \cdot \vec{t}_2 \times \vec{t}_3}$$

following the given explanation,  $T_3$  corresponds to  $2\pi$  divided by the minimum distance between planes formed by  $\vec{t}_1 \times \vec{t}_2$ .



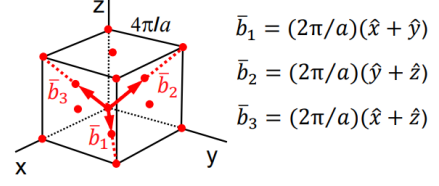
Source: Rumpf<sup>19</sup>

(a) In this figure contiguous planes formed by  $\vec{t}_1 \times \vec{t}_2$  defines the reciprocal vector



Source: Cantero<sup>20</sup>

(b) Reciprocal( $\vec{b}_j$ ) and real lattice vectors( $\vec{a}_i$ ) for a FCC lattice.



$$\vec{b}_1 = (2\pi/a)(\hat{x} + \hat{y})$$

$$\vec{b}_2 = (2\pi/a)(\hat{y} + \hat{z})$$

$$\vec{b}_3 = (2\pi/a)(\hat{x} + \hat{z})$$

**Figure 2.7:** Reciprocal and real lattice concepts.

### 2.3.2 Band structure and functioning of BandSOLVE

The BandSOLVE solves the light propagation modes that can exist within a photonic structure. Specifically, assuming linear response, lossless and isotropic materials, the program look for time-independent solutions assuming a factor  $e^{-i\omega t}$  as the temporal part of wave solutions. Additionally, due to lattice symmetry postulations, Bloch's theorem can be applied too. This theorem says that the waves that can propagate in a periodic lattice are harmonic waves( $e^{ikx}$ ) multiplied by a function that must store the periodic permittivity characteristics of the lattice( $u_k(x)$ ). In this context, the wave vector  $k$  is also called the Bloch wave vector and corresponds to a wavelength equal to  $2\pi/k$ .

All these considerations are introduced into Maxwell's laws which leads to the final equation that is responsible for solving BandSOLVE<sup>21</sup>:

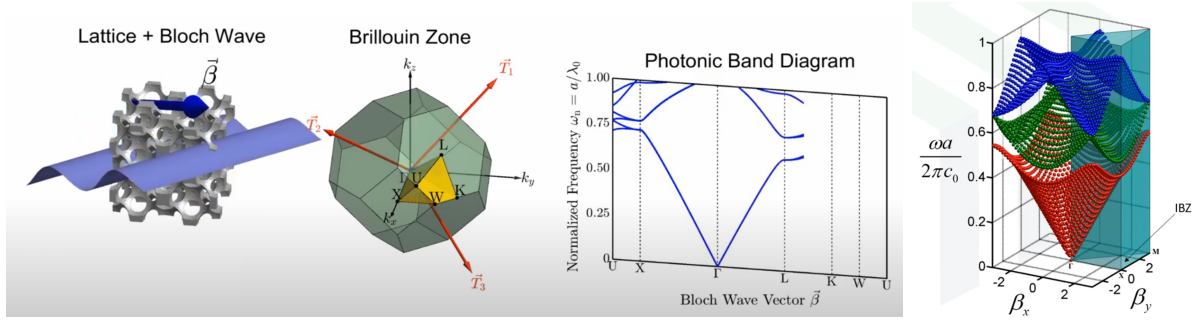
$$\left. \begin{array}{l} \text{Maxwell equations: } \vec{\nabla} \times \left( \frac{1}{\epsilon(x)} \vec{\nabla} \times \vec{H}(x) \right) = \frac{\omega^2}{c^2} \vec{H}(x) \\ \text{Bloch Theorem: } \vec{H}(x) = e^{ikx} \vec{u}_k(x) \end{array} \right\} \Rightarrow$$

$$(i\vec{k} + \vec{\nabla}) \times \left( \frac{1}{\epsilon(x)} (i\vec{k} + \vec{\nabla}) \right) \times \vec{u}_k(x) = \frac{\omega^2}{c^2} \vec{u}_k(x) \quad (2.5)$$

Also, once the magnetic field is obtained, the complementary electric component of the light can be easily obtained using another time Maxwell equations:

$$\vec{E}(x) = \frac{i}{\omega \epsilon_0 \epsilon(x)} \vec{\nabla} \times \vec{H}(x)$$

The main equation 2.5 corresponds to an eigenvalue equation, equivalent to the quantum operators acting on a quantum state. Thus, given a wave vector  $k$ , and obviously fixing the permittivity structure, we will obtain as eigenvalues the normalised frequencies ( $\omega^2/c^2$ ) for the eigenvectors  $u_k$ . In fact, given a wave vector, we can obtain infinite number of solutions  $W_{k,n}$  labeled by the band number  $n$  in order of increasing



Source: Rumpf<sup>22</sup>

**Figure 2.8:** Lattice, Bloch wave vector in real and reciprocal space, and the resulting band structure. The inputs for BandSOLVE are the lattice and the Bloch wave vector, the output is a Band Diagram like the two right figures.

frequencies. Additionally, this frequency values will be given by means of a dimensionless value in results discussion section:

$$\omega a / 2\pi c = a / \lambda \quad (2.6)$$

where  $\lambda$  is the free-space wavelength in contrast to that obtained with  $2\pi/k$ , which corresponds with the wavelength in the lattice medium. The wavelength in free space is the interesting parameter as normally the experimental lasers are emitting in an air medium ( $n \simeq 1$  as in vacuum) before hitting the sample. The two wavelengths are related by the effective index, defined as the average refractive index that the wave sees in the lattice:  $\lambda = n_{ef}(\frac{2\pi}{k})$ .

To characterise the propagation modes of the lattice, it would be necessary to cover the entire first Brillouin zone, in order to consider all possible Bloch vectors in the lattice. In the 2D case, BandSOLVE would give us frequency mode surfaces as shown in the right corner of figure 2.8. These surfaces are called bands and they all correspond to the same band number, the set of surfaces forms the band structure. In addition, if two adjacent bands do not touch at any point in the Brillouin zone, there is a range of frequencies where doesn't exist light propagation in the lattice. This zone is called a photonic bandgap (PBG).

Normally, as the objective is to find and optimise PBGs, it is not necessary to solve the whole first Brillouin zone. Thanks to group theory it can be proved that the extreme points of the bands occur at points of high symmetry, these points are at the edges of the IBZ. On the right-hand side of figure 2.8 the volume covered by the IBZ can be seen coloured blue. On the perimeter of this zone, high symmetry points can be found labeled as  $L, M, \Gamma$ . Therefore, in order to identify and study PBGs, it is enough to perform BandSOLVE simulation through these symmetry points along the perimeter, forming the typical band diagram shown in the right center of figure 2.8.

Now, the general solutions obtained do not have a defined polarization of the electric and magnetic field and in general these can have non-zero components in all three dimensions, this are called hybrid modes. However, in photonic lattices with 1D or 2D symmetry it is possible to classify the propagation modes also according to two modes of polarization of the light: TE and TM. Following the convention established by RSoft CAD, TE modes correspond to modes in which the electric field oscillations do not see



the periodicity of the structure because they are travelling in the longitudinal direction of the lattice. On the other hand, TM modes are those light waves where, in this case, it is the magnetic field that oscillates in the longitudinal direction of the lattice. Figure 2.9 shows the direction of vibration of the EM fields of these modes in the case of the 2D symmetric hexagonal lattice of pores.

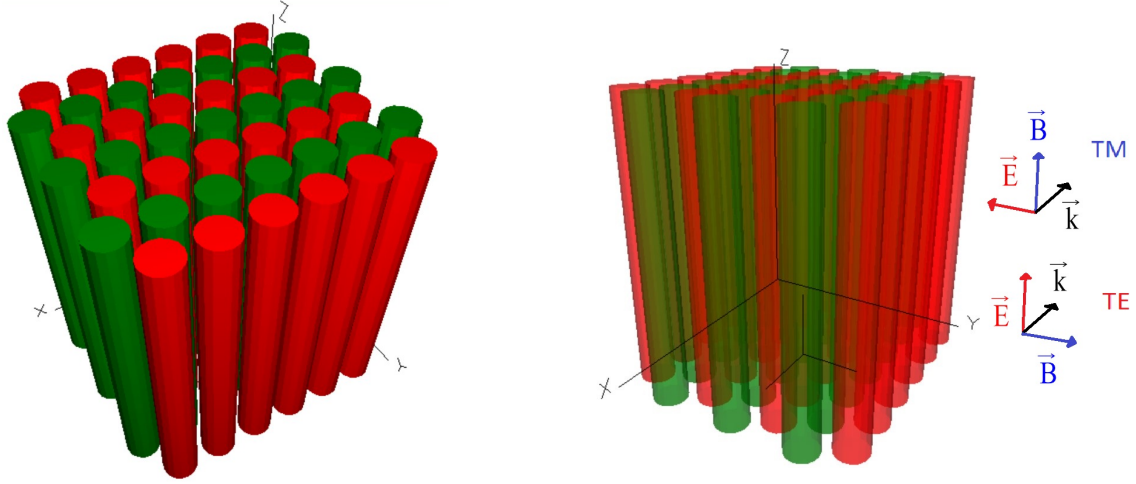


**Figure 2.9:** Propagation modes for a longitudinally extended hexagonal lattice of pores. These propagation modes are defined in 1D and 2D but can be extended to three-dimensional lattices which are symmetric along one of the axes, z axis in this case.

To conclude this subsection, it is also important to mention the use of the MOST tool. It is a simulation program within RSoft CAD and, like BandSOLVE, it allows to obtain the light modes present in the lattice. However, its advantage is that it is possible to add an action macro in order to obtain different partial results of the band structure, like the first bandgap, depending on lattice parameters, such as in our studied case the diameter of the air pores. Moreover, MOST allows the visualisation of the distribution of the EM fields associated with the modes for a given wave vector  $\vec{k}$ , which will be useful for studying a waveguide.

### 2.3.3 Hexagonal lattice with BandSOLVE

For the work done in BandSOLVE, a hexagonal air nanopore lattice in YAG with 1  $\mu m$  lattice parameter has been created with RSoft CAD. Its structure was represented in figure 2.9, and in figure 2.10 can be seen the corresponding conventional cell and lattice vectors in a cross section representation.

The conventional work cell<sup>1</sup> considered in figure 2.10 does not correspond to the primitive cell as it has three lattice points per cell. However, taking into account that the filling factor (FF) is defined as the quotient between the area occupied by the lattice points ( $A_{pr}$ ) and the total area of the lattice ( $A_r$ ), its expression for the case of the hexagonal lattice is obtained in a simple way from this conventional cell. Thus, inside the cell are identified three pores of radius 'r' within a total area of the cell equivalent

<sup>1</sup>Conventional cells are larger than primitives but they still have the property of covering the whole lattice from their repeats. Their advantage is that they can be easier to make calculations.

to 6 equilateral triangles of base equal to the lattice parameter 'a' and height ' $\frac{\sqrt{3}}{2}a$ '. Therefore, the FF is:

$$FF = \frac{A_{pr}}{A_r} = \frac{3 \cdot (\pi r^2)}{6 \cdot \frac{\sqrt{3}/2 a \cdot a}{2}} = \frac{2\pi}{\sqrt{3}} \left(\frac{r}{a}\right)^2 \quad (2.7)$$

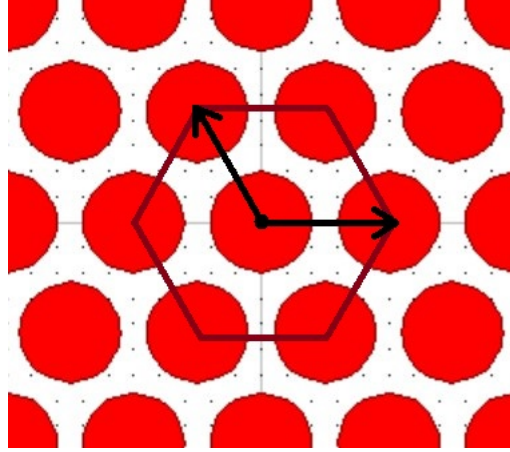


**Figure 2.10:** Pore lattice forming a hexagonal structure. The hexagon corresponds to the conventional cell and the two black arrows to the lattice vectors.

## 3. Results discussion

---

### *Resumen*

---

En este tercer capítulo se presentarán y discutirán los resultados obtenidos en cristal YAG para los nanoporos de aire fabricados y el cambio de índice de refracción obtenido en zona litografiada. Además, se analizarán las estructuras de bandas para una red hexagonal de poros y los modos de propagación en una guía de onda, ambos simulados con BandSOLVE.

---

This third chapter will present and discuss the results obtained in YAG crystal for the fabricated air nanopores and the refractive index change obtained in laser-written zones. In addition, band structures for a hexagonal lattice of pores and propagation modes in a waveguide will be analysed, both simulated with BandSOLVE.

### 3.1. Pore Characterization

Air pores were fabricated using technique presented in methodology. The aim in this section is to analyse the length and shapes of wet-etched pores for different laser-written configurations.

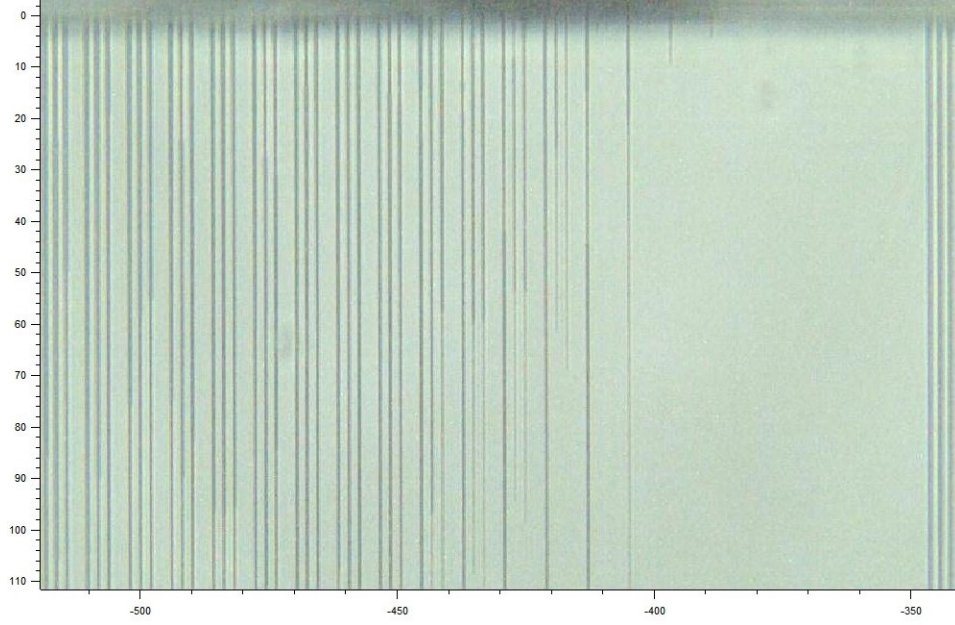
#### 3.1.1 Pore length study at equal etching time

To identify the best configurations to fabricate hollow nanopores with the highest etching rates, an experiment was done using 3DLW technique to write straight lines at different writing speeds, pulse energies and laser pulse repetitions in YAG crystal. After laser lithography, they were chemically etched for 41 hours. Exactly, the following writing combinations were made:

Set of speeds	Pulse Frequency	Pulse Energy(nJ)	Abbreviation
1	1 kHz	20	1k20
	10kHz	20	10k20
	10kHz	17	10k17
	100kHz	19	100k19
2	1MHz	17	1M17

**Table 3.1:** Different combination sets done with 3DLW technique.

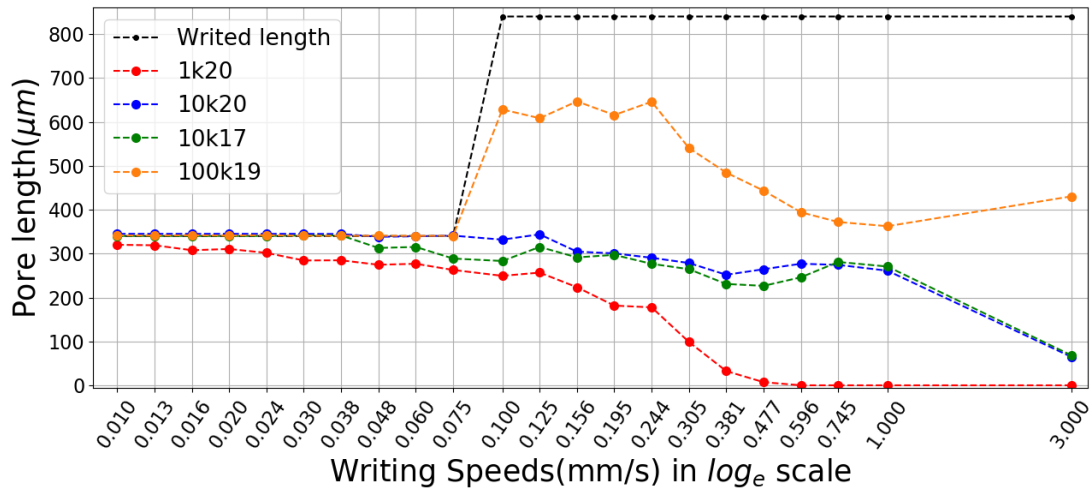
As the laser traces the lines in succession, there are two equal lines for each combination of parameters. This is because the laser draws one line out and one line back to return to the same height on the sample. Thus, all measure with a specific combination of speeds, frequencies and energies are duplicated.



**Figure 3.1:** Pores 41h wet-etched with 1k20 set in YAG.

In figure 3.1 is presented some pores created for the 1k20 case. Groups of three pores can be seen. This is because, in fact, at the same writing speed, a third trace is done, overwriting in the forward and backward direction. However, this third line isn't studied in this work. In addition, three perfect lines can be seen on the right side of the image. These lines are security traces made in a combination of parameters that are known to etch the pores well<sup>9</sup>.

The length measured for the forward traces are represented in the following figure 3.2. Also, in figure 3.3 are the results for the backward traces.



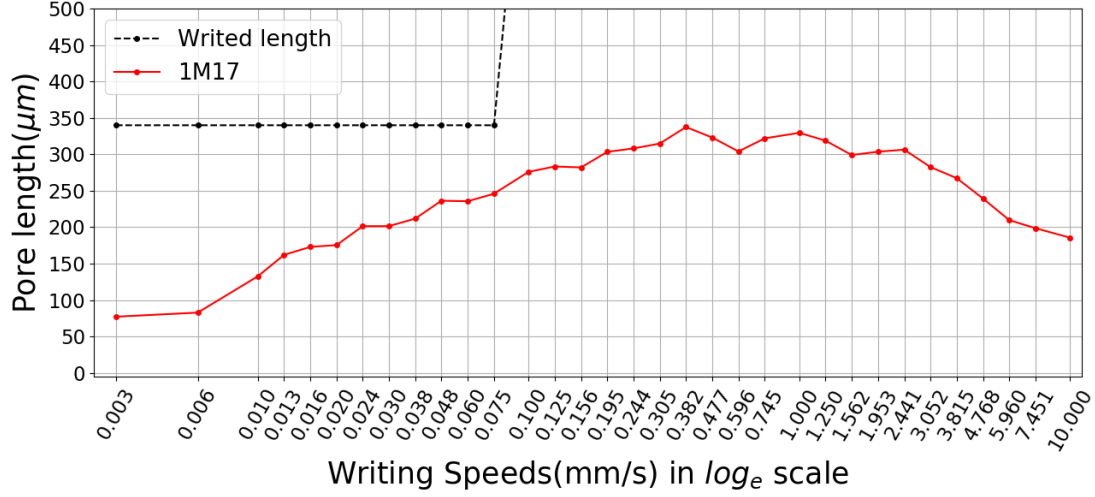


**Figure 3.2:** Forward traces for 41h wet-etching pores as a function of writing velocities

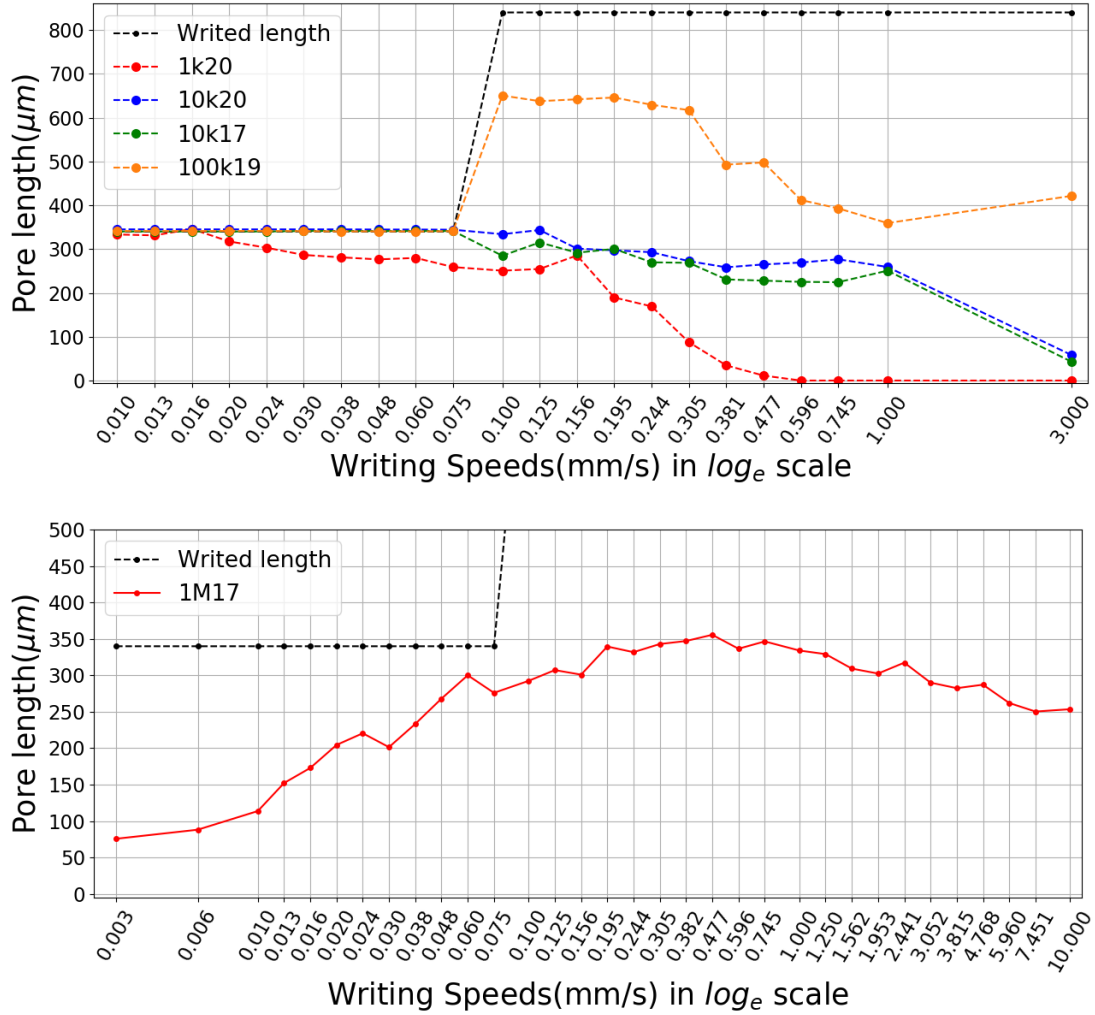


**Figure 3.3:** Backward traces for 41h wet-etching pores as a function of writing velocities

The discussion of figures 3.2 and 3.3 is centred in the pore overlapping phenomenon. If the laser pulses are emitted closer together in the sample, the overlapping will be

greater. This parameter will therefore depend on the frequency of the pulses as well as the writing speed.

Three behaviours can be identified. At low overlapping, the pore is not lithographed with sufficient continuity for the chemical etching to occur properly. On the other hand, at high overlapping, the spatial density of pulses is so high that can occur the complete breaking of electronic bonds making chemical etching difficult. The middle point is the most suitable, where the crystall bonds are sufficiently modified but not broken, favouring the chemical attack.

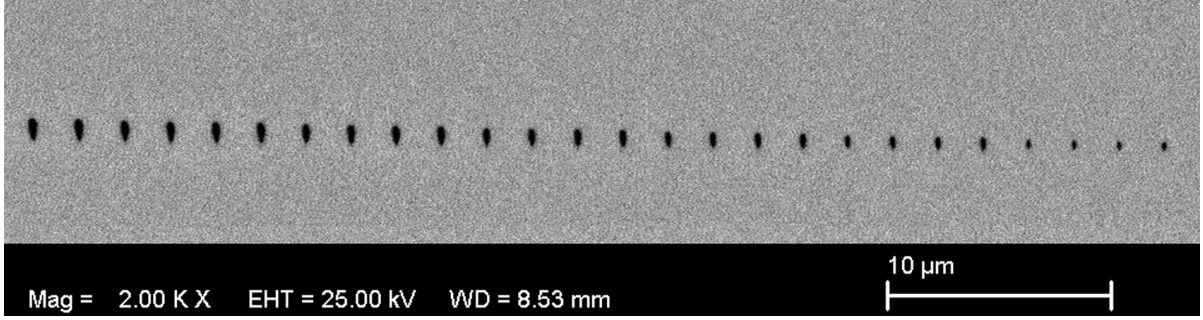
These three regimes can be observed for the figures of 1M17, where the etched length is maximum for  $\sim 0.45\text{mm/s}$  writing speed. Above all, the decrease of pore length at low speeds, due to very high overlapping, is clearly observed. As 1MHz is a really high frequency, the length pore decay at high speeds is partially seen, as the overlapping isn't low enough yet.

In the other laser configurations, the high overlapping zone cannot be discussed as the entire lithographed zone was etched for low writing speeds. Thus, it isn't possible to identify the optimum scan velocity for this configurations. However, it can be seen lower pore lengths at high speeds due to the low pulse "densities" in the material.

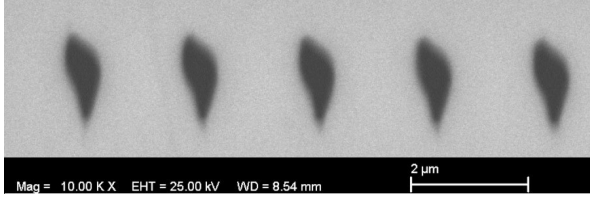
### 3.1.2 Pore width and height analysis.

Now, the transverse plane of the pores is studied with images done via SEM. Due to external problems, the microscope was under repair during the course. Therefore, these images were given by the Tutor Airán Ródenas from past measurements. All the pores analysed were previously lithographed with 3DLW at 1MHz pulse repetition, 1mm/s writing speed and in the same direction. Also, these pores have all the same chemical etching time and the energy pulse used is reduced to the right every four pores. In figure 3.4 is showed the SEM images taken. Only part of the pore array is shown, as this is the only part to be analysed in this work.

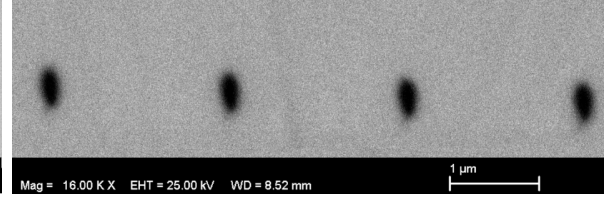
The analysis of this pores is done with FIJI ImageJ software, described in methodology. The parameters measured are the area, the perimeter and, fitting the pores to an ellipse, the major and minor axis. In table 3.2 the averages of the sets of 4 equally written pores with their errors given by the standard deviation are presented (all measurements made are shown in appendix A). The labelling used for the sets goes from highest to lowest pulse energy and the ellipticity is also calculated with its error by doing error propagation<sup>23</sup> (go to appendix B to see the formula used).



(a) Right edge of the pore array.



(b) First four pores



(c) Last four pores

**Figure 3.4:** SEM images for the transversal plane of pores varying energy pulses every four pores

Pores set	Area( $nm^2$ )	Perim.( $nm$ )	Major( $nm$ )	Minor( $nm$ )	Major/minor
1	$429000 \pm 5500$	$3080 \pm 20$	$1196 \pm 14$	$457 \pm 7$	$2.62 \pm 0.07$
2	$441000 \pm 4700$	$3120 \pm 40$	$1214 \pm 5$	$463 \pm 4$	$2.62 \pm 0.03$
3	$445000 \pm 6000$	$3130 \pm 60$	$1208 \pm 9$	$469 \pm 7$	$2.58 \pm 0.06$
4	$443000 \pm 3400$	$3130 \pm 40$	$1203 \pm 11$	$469 \pm 7$	$2.57 \pm 0.06$
5	$411000 \pm 18000$	$2970 \pm 60$	$1148 \pm 21$	$456 \pm 15$	$2.52 \pm 0.13$
6	$121000 \pm 2600$	$1660 \pm 70$	$631 \pm 11$	$245 \pm 2$	$2.58 \pm 0.07$
7	$89000 \pm 3000$	$1390 \pm 30$	$521 \pm 15$	$217 \pm 5$	$2.4 \pm 0.12$
8	$43000 \pm 3500$	$910 \pm 60$	$333 \pm 17$	$165 \pm 6$	$2.02 \pm 0.18$

**Table 3.2:** Cross-sectional measurements of pores.

As can be seen in table 3.2 and figures 3.4, lower energies induce lower pore sizes. Additionally, the pores made with lower energies have a more rounded shape, although they still have an ellipticity of  $\sim 2$ . So, if we want pores with 2D symmetry to create efficiency photonic structures or microstructured optical waveguides (MOWs), this could be achieved by reducing pulse energies used. However, if the pulse energy is greatly reduced, the material is not nano-modified and therefore these hollow pores are not created by wet-etching. Also, if larger pore diameters were required with the same cross-section shape, increasing etching time will induces bigger sizes but with a small etching rate.

Beside this experiment, the minimum pore size was observed reducing the energy pulses more and more. Thus, the limiting pore heights and widths obtained with this



technique are below hundreds of nanometres. They correspond exactly to  $(82 \pm 7 \text{ nm})$  x  $(58 \pm 7 \text{ nm})$  and therefore have an ellipticity of  $1.41 \pm 0.29$ , even smaller than those observed in the table and corroborating the rounding of pores as the energy decreases. In figure 3.5 is shown this pore discussed.

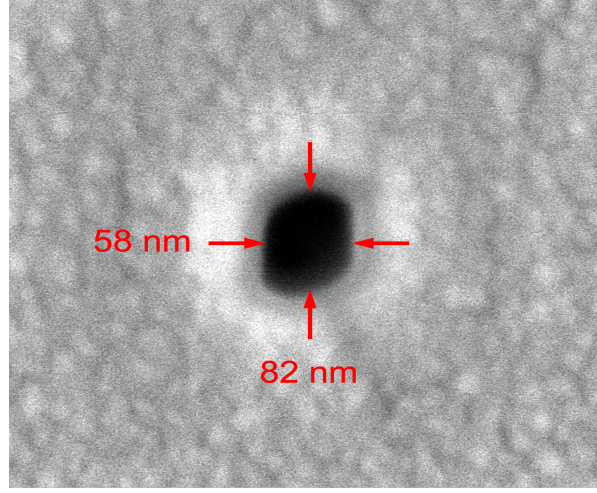


**Figure 3.5:** Minimum size limits achieved for the wet-etched nanopores.

## 3.2. Refractive index in lithographed zoned

Using the WFPI technique, in this section the index change in the YAG within the 3DLW zone is characterised. To facilitate the measurement, a plane extended on the Y-axis and  $50 \mu\text{m}$  width in X is written. For this purpose, consecutive lines along the Y-axis and spaced  $25 \text{ nm}$  distant on the X-axis are written at a speed of  $1 \text{ mm/s}$ ,  $1 \text{ MHz}$  repetition frequency and 3 pulses per window, so the laser emits always 3 pulses in a row. The total power is  $17 \text{ mW}$  of power, which, knowing the repetition frequency and pulse per window, is equivalent to a pulse energy of  $5.7 \text{ nJ}$ . A microscope reflection photograph of this plane is shown in figure 3.6. It is taken with a  $100\times$  objective.

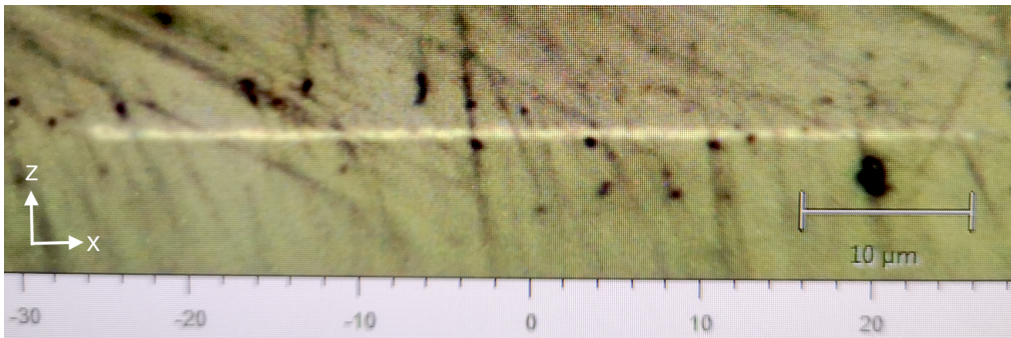


**Figure 3.6:** Raman photography of the written plane in the XZ view. It is taken with  $100\times$  objective in reflection.

In figure 3.7 is presented the two images taken with WFPI and the resulting OPD map. The change in the refractive index seem appreciable in this figure, where in  $x \simeq 60 \mu\text{m}$  and  $x \simeq 110 \mu\text{m}$  are the edges of the written plane. Also, the right zone of this plane has to be disregarded in the analysis since a failed plane is lithographed there. Between



110 and 160 micrometers can be seen a roughness in OPD colour map that corresponds to this wrongly written map.

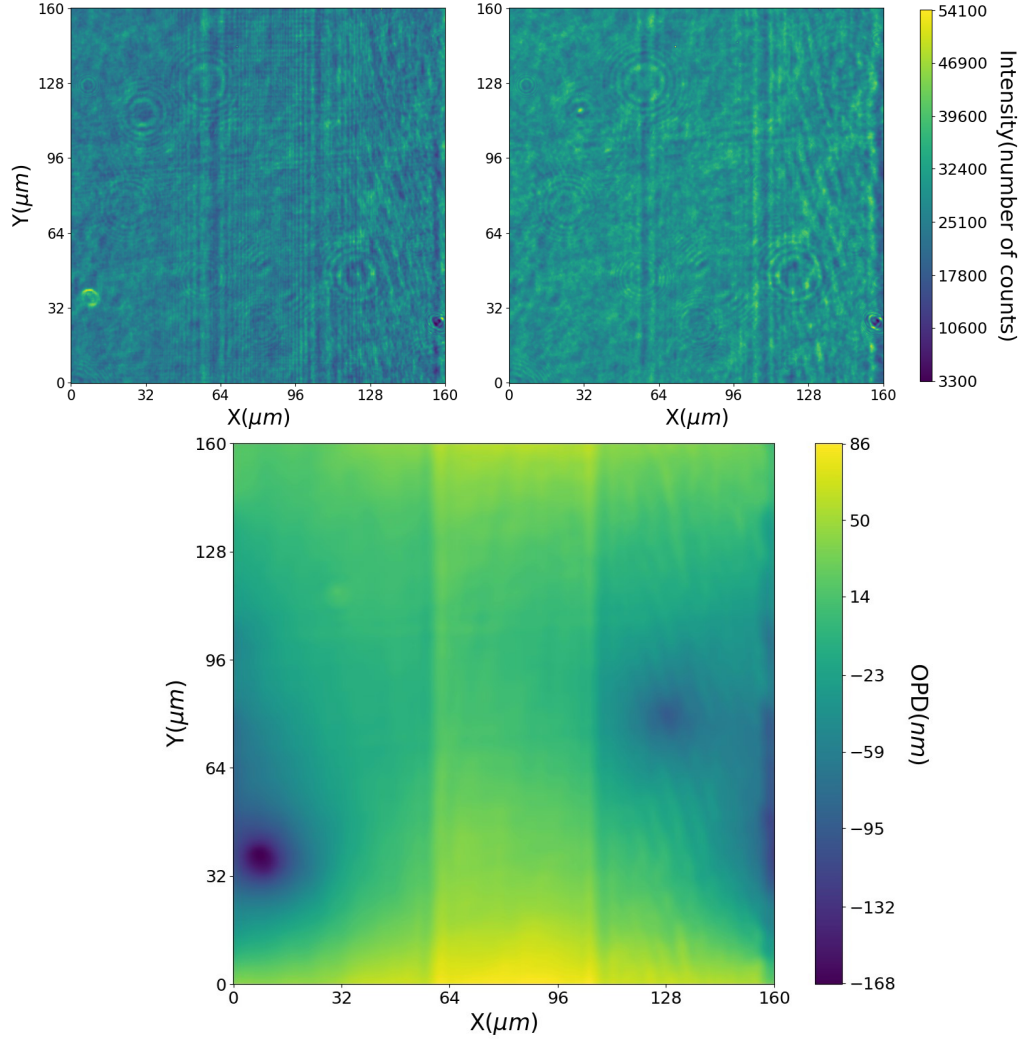


**Figure 3.7:** Intensity images used for OPD reconstruction and the resulting OPD map.

To analyse the optical path jump in the plane, the average profile along the x-axis is calculated and plotted in figure 3.8. In addition, the standard deviation and averages for sub-intervals on the y-axes are also represented. As can be seen, the average profile captures the lithographed area in the form of a "plateau" and it will be useful for calculating the optical path difference by the change of the index. Furthermore, visualising the partial averages and the standard deviation, the OPD profile changes significantly depending on the region on the Y-axis averaged. This is because the crystal is not completely homogeneity and flat on its faces. On the other hand, there is an standard deviation 'offset', that affects all the X-axes equally, due to the instrumental error, and it's equal to  $\sim 16nm$ <sup>1</sup>, which is important. The OPD fluctuations can be observed especially large at the beginning and at the end of the X-axis in figure 3.7, but explicitly in figure 3.8. Luckily, in the central region on the X-axis, where the written area is located, the standard deviation is not as large as in the edges of the axis.

<sup>1</sup>Making the coarse assumption that the minimum of the standard deviation profile along X is equal to the instrumental error. Therefore, the roughness of the material is supposed to 0 in this point.

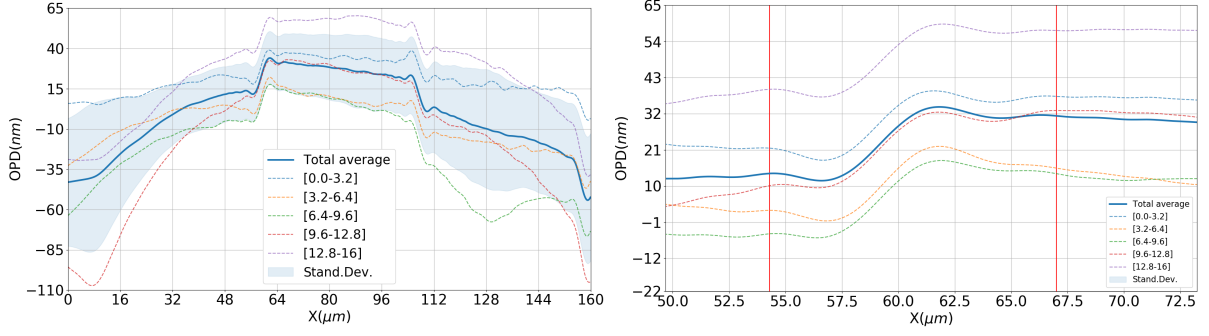


**Figure 3.8:** OPD profile along X-axis. In the legend are presented the Y-intervals in millimetres used to calculate sub-average the profile. Also it is showed the standard deviation of the full average profile. The right figure corresponds to a zoom in the OPD jump due to written plane.

The OPD due to laser in the lithographed area has to be calculated in comparison to the nearest area without writing, in order to achieve the smallest difference in the homogeneity of the crystal. Looking at figure 3.8, the two red vertical lines seem to be the best places where the irregularities on the edge of the written plane have ended and therefore it is more correct to calculate this value. Thus, OPD due to 3DLW can be calculated, averaging along the Y-axis, the rest between the OPD values in the x positions given by the two vertical red lines:

$$OPD_{3DLW} = \int_{y=0}^{y=160} \frac{OPD(x = 67, y) - OPD(x = 54, y)}{160} dy \quad (3.1)$$

where x and y are expressed in micrometres. This integral is actually approximated with a Riemann sum due to sampling minimal size in the CCD detector.

The value obtained is  $18 \pm 10\text{nm}$ , where the error is taken with simple error propagation of the instrumental error (5nm). Also, the standard deviation value is 4 nm, one third of the value of the error taken, which demonstrate the resolution of the instrument.

To obtain now the change in refractive index, it is also necessary to know the z-thickness of the plane. In the absence of SEM images, it is considered a typical value of  $300 \pm 10\text{nm}$ <sup>2</sup>. With all this, and using equation 2.3, it is now possible to calculate the index change with his error (propagation error formula in Appendix B):

$$\Delta n = 5.9 \pm 3.5 \cdot 10^{-2}$$

Thus, the error in the index change is significantly high compared to its value, so the measurement is not as good as desired. In any case, it seems to indicate that the YAG index, 1.846 for the wavelength used in WFPI, suffer a change value in its second decimal order when 3DLW is done in this configuration. This effect implies that optical guiding structures based on step-index guiding (SIF) can be engineered also by this technique. This has been studied previously with also 3DLW technique but in other configurations and materials substantially different<sup>24</sup>.

<sup>2</sup>This value is based on previous 3DLWs SEM images with similar characteristics.

### 3.3. Pore Hexagonal lattice: Band structures and wave guides

In this section, the results obtained with the hexagonal lattice of air nanopores in the YAG crystal are presented. Exactly, the band structures and a waveguide with this lattice as cladding are analysed with numerical solutions, thanks to the BANDSOLVE software. Finally, a hexagonal lattice realised in the laboratory is also presented for a first approach to the structures studied in this section.

#### 3.3.1 2D model: Bandgaps

Firstly, without including the longitudinal pores direction in the program, the two-dimensional hexagonal lattice with a lattice parameter of  $1\mu m$  is analysed in order to find the pore radius for which the photonic bandgap (PBG) is the largest. This lattice and its propagation modes (TE,TM) were previously represented in figures 2.9 and 2.10.

The domain over RSoft will perform the simulations will be the minimum for which the program reproduces the periodicity of the lattice faithfully and thus optimises the time of calculation. As it was discussed in section 2.3.2, for the PBG analysis it will only be necessary to scan the K vector through the symmetry points along the perimeter of the IBZ. Both, the domain in real space and the reciprocal space used, are presented in the figure below:

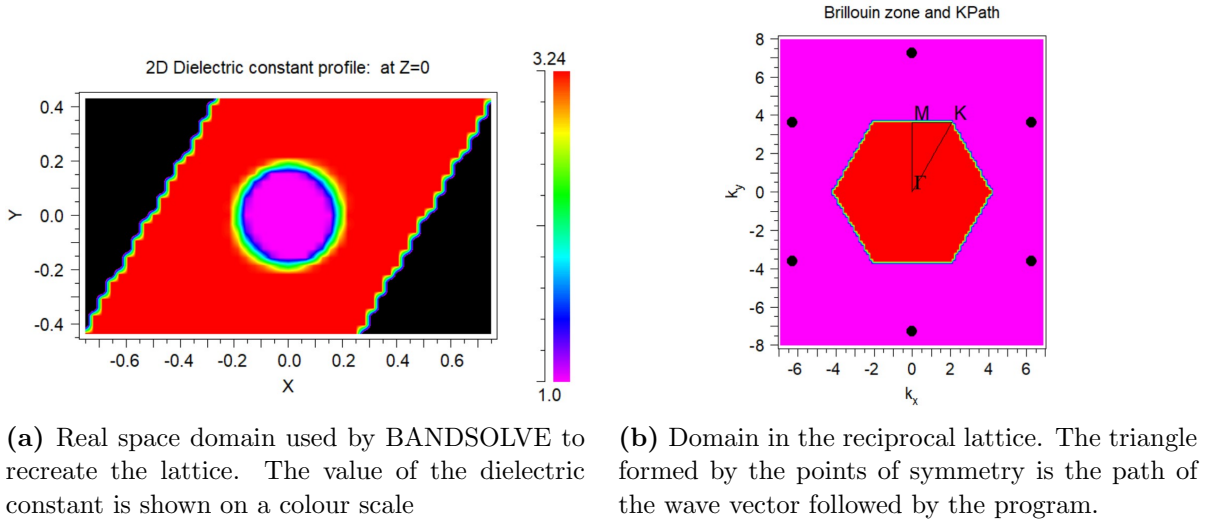
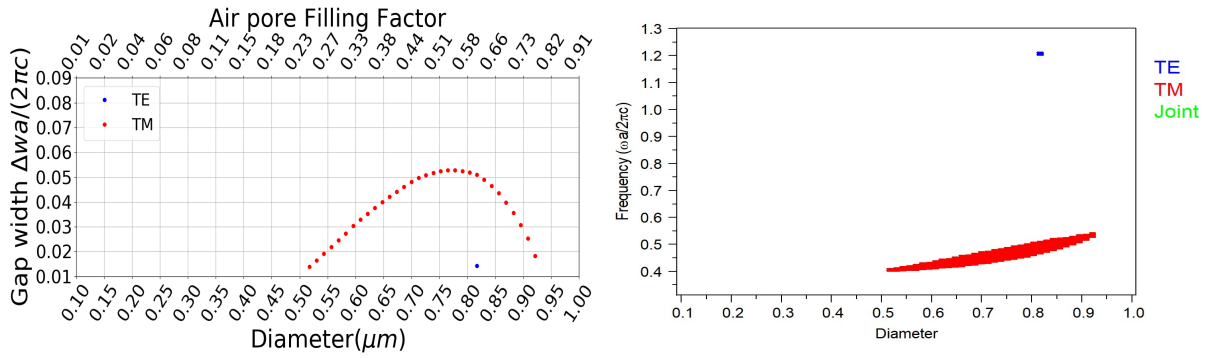


**Figure 3.9:** Real and reciprocal space domains of the hexagonal lattice for lattice parameter  $1\mu m$  and pore diameter  $0.375\mu m$ .

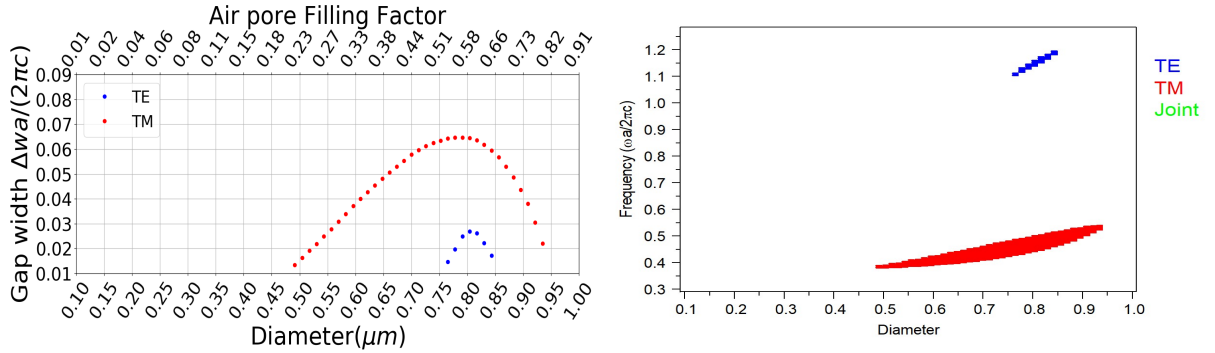
The optimisation is carried out for the values of first bandgap width using the MOST tool, as we can include the pore radius as a sample variable. In addition to the bandgap width, the gap map is obtained. This process is repeated for different spectral ranges of YAG (MIR, NIR, VIS, UV), since the refractive index of YAG depends on the wavelength<sup>17</sup>.

The results are presented in figure 3.10. As it was said in methodology, the frequency values, given on the y-axis of this figure and the following, are normalised to be dimensionless. In this figure, the TE modes show hardly any bandgap for the first frequency modes. However, as the refractive index of YAG increases (for lower wave lengths), larger ranges of diameters with bandgaps are found in the TE mode.

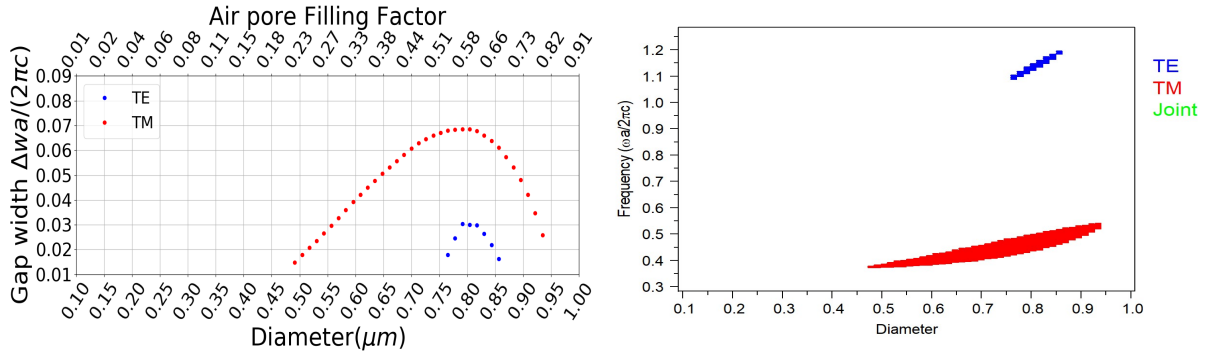
On the other hand, the TM modes, in which the electric field oscillates within the plane of the pore cross-section, show a bandgap over a larger range of pore diameters, generally starting from half a micrometre. In addition, these bandgap widths have a higher value than those found for TE polarization. Therefore, it is more interesting to focus on the bandgap TM as it is better for example for fabricating forbidden band photonic crystal fibers (PCFs).



(a)  $n=1.72$ , MIR(5000nm)



(b)  $n=1.807$ , NIR(1500nm)



(c)  $n=1.837$ , VIS(530nm)

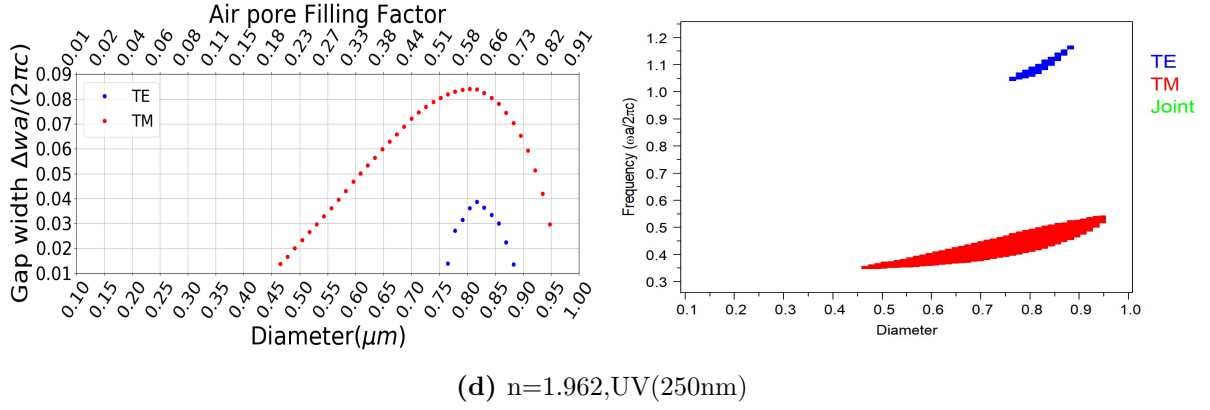


**Figure 3.10:** Gap map and width of the first band gap for TE and TM modes as a function of air pore diameter, results for the different spectral ranges of YAG. The band gap width is given as a normalised frequency incremental, for gap map as normalised frequencies. The diameters are all in microns

The results for TM modes are summarised in the figure 3.11, where the corresponding lattice for some pore diameters are also represented. As can be seen in this figure, the approximate diameter for which the bandgap is largest varies slightly with the spectral range considered. For the longest wavelengths, in the MIR, this maximum is at 0.75 microns. On the other hand, for the shorter wavelengths the optimum diameter increases as the bandgap width increases, until it reaches the last spectral range scanned, the UV, where the pore diameter is 0.8 microns and the bandgap width 0.085. This diameter range is equivalent to a FF of [0.51-0.58], which is relatively large air content as can be seen in the 0.8 microns diameter lattice plotted within the figure.

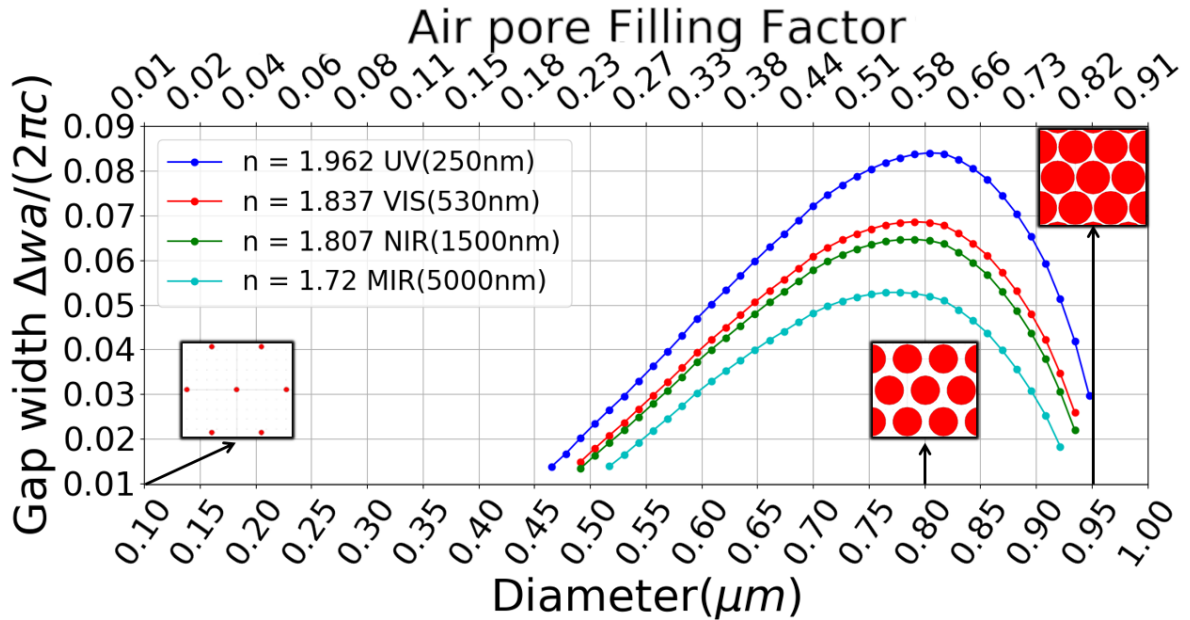


**Figure 3.11:** Bandgap width of TM modes as a function of diameter for different spectral ranges.



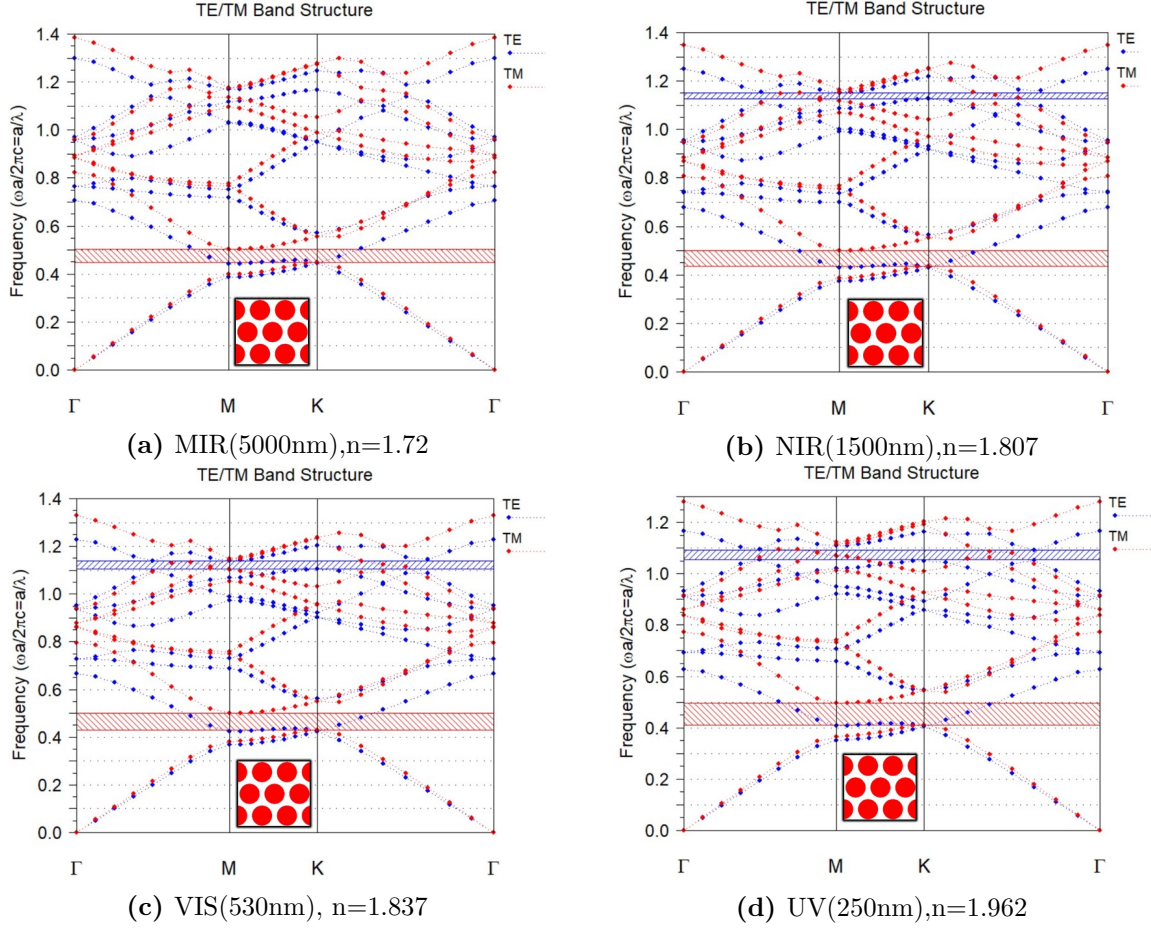


**Figure 3.12:** Band structure for the pore diameter with the highest bandgap in the different YAG spectral ranges

Now, the band diagrams corresponding to the pore diameters for which the gap width is the largest are plotted in figure 3.12. As can be seen, the centre of the bandgap, in terms of dimensionless frequency, decreases slightly as we move to shorter wavelength spectral ranges. For the MIR this bandgap is centred at 0.47, while in the UV it is at 0.45. Using equation 2.6 and with  $1\mu\text{m}$  lattice parameter, this frequencies corresponds to a free-space wavelength  $\lambda$  of  $\sim 2150\mu\text{m}$ .

### 3.3.2 3D model: bandgaps in longitudinal direction

Once the PBGs that present this lattice have been studied, we proceed to take the same type of lattice but in three-dimensional space. In this case the lattice will correspond to the one previously shown in the figure 2.9 where the domain in real space as in the reciprocal used for the calculation of bands by BANDSOLVE are totally equivalent to those shown in the figure 3.9.

If one were to recalculate the band structures of this lattice in this 3D model lattice, one would see that they are exactly the same results as shown above. This is obvious, as Rsoft CAD runs the 2D model as a 3D pore lattice but with an infinite longitudinal z-size. Therefore, with this 3D model a finite size is given to the pores and also the

Bloch vector can be scanned through the z-direction<sup>3</sup>, which is the aim of this section.

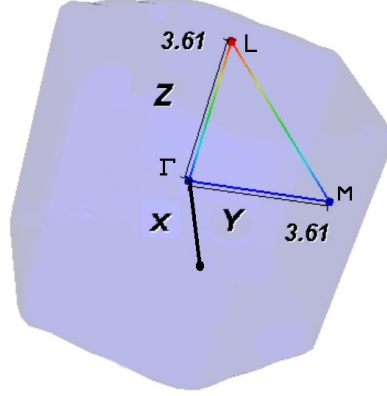


**Figure 3.13:** New path followed in the scanning of wave vectors to elaborate the band structure.

Thus, instead of using the path given in figure 3.9(b) we will also have to traverse the third dimension to consider the longitudinal direction of the pores in order to see the behaviour of the band structure in this direction. Therefore, the new path followed will touch, in addition to the symmetry points  $M$  and  $\Gamma$ , a new point which I define as  $L$  and which will correspond to the longitudinal direction of the pores. For illustrative purposes, the path followed inside the first Brillouin zone is represented in figure 3.13.

This new Bloch wave direction toward  $L$  causes the loss of the previous transverse symmetry of the lattice to the wave vector and, thus, classifying into TE and TM modes is not possible now. Therefore, in this case there are hybrid bands.

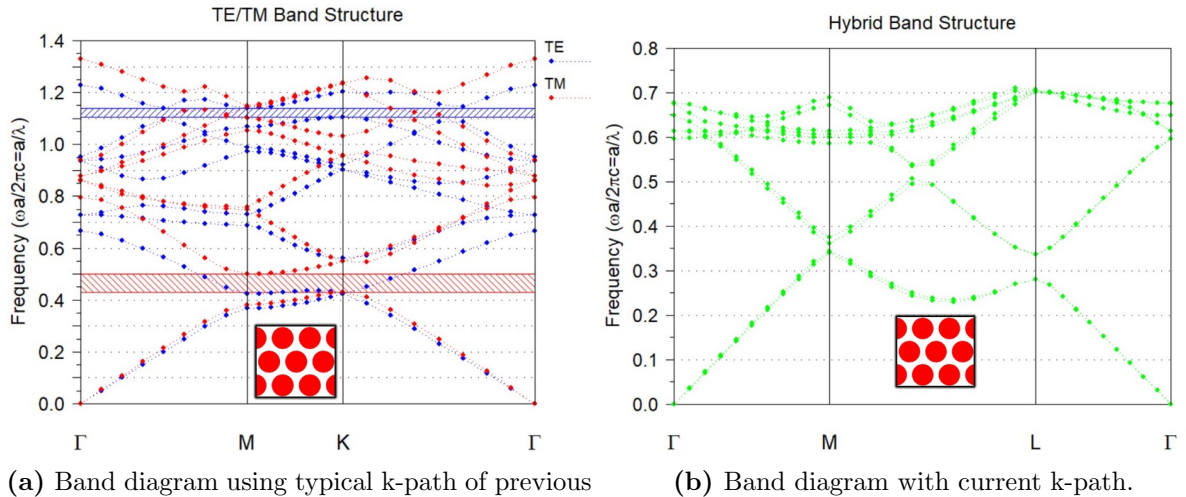


**Figure 3.14:** Band diagram using two different k-paths.

<sup>3</sup>Actually, in 2D hexagonal lattice it is also possible to calculate the frequency modes in z-direction. However, it does not allow a complete scan like the one shown in figure 3.13

The band structure, presented in figure 3.14, was made for the VIS region of the YAG where the refractive index is 1.837. In addition, the optimised pore diameter value was chosen in order to compare with the band structure results already done. It can be seen that when the wave vector is directed to the longitudinal direction the bandgap is lost. Although, for a frequency of 0.35 it may be possible that, by doing the numerical calculation with higher resolution, a small bandgap can be identified at this point. Moreover, it is interesting to observe how the band structure coincides with that obtained with the previous k path for the common symmetry points  $\Gamma$  and M. As one would expect, the TM and TE bands is only a classification that can be made in the transverse direction, therefore, the frequencies obtained in this equivalent range of k-path should remain the same in both figures.

### 3.3.3 Analysis of a Microstructured Optical Waveguide

In this subsection the 2D model of the hexagonal lattice, with a lattice spacing  $a = 1\mu m$  and a pore diameter of  $0.79\mu m$ , is considered. The notation now is that the cross sectional plane now extends in the XZ plane. The aim is to learn how to identify waveguide modes, differentiate between each, and see their spatial intensity distribution as well as effective indices. For this purpose, a single nanopore is removed from the nanopore lattice creating a dielectric cavity which would act as core region, with a waveguide cladding composed of the pore lattice, with light propagating along the nanopore direction and with light polarization within the lattice plane. In the waveguide core, the light will be guided in high index region created by the defect within the periodic crystal structure. This light remains guided within the core due to the index difference between the core and the cladding medium, which is nanostructured. In this respect, guiding is expected to be maintained mainly due to the total internal reflection between the core and the cladding. The presence or not of photonic bandgaps (PBGs) within the cladding is not further analysed in this work. Although it can be seen from the previous bandgap study (see figure 3.12), that if the wavelength has to resonate with the cladding TM bandgap for  $a = 1\mu m$ , the modes would need to be at wavelength of  $\sim 2\mu m$  in free space. However, because the wavelength of interest for YAG is of around  $1\mu m$ , work was done with a normal waveguide in this spectral range, in which refractive index of the YAG is 1.82. Further work can be done by reducing the lattice spacing to  $a=500nm$  in order to consider the PBG studied, but such study could not be done due to lack of time.

In order to also detect possible erroneous results of the propagation modes given by bandsolve, two periodic integration domains are considered for comparison. As it was said, these domains are used by bandsolve as building blocks to form the entire lattice.

#### First integration domain

Figure 3.15 shows the first periodic integration domain imposed on Bandsolve. The idea is to take as many pores as possible so that, during the calculation, as this domain repeats to form the whole lattice, the waveguide only sees one defect in the centre.



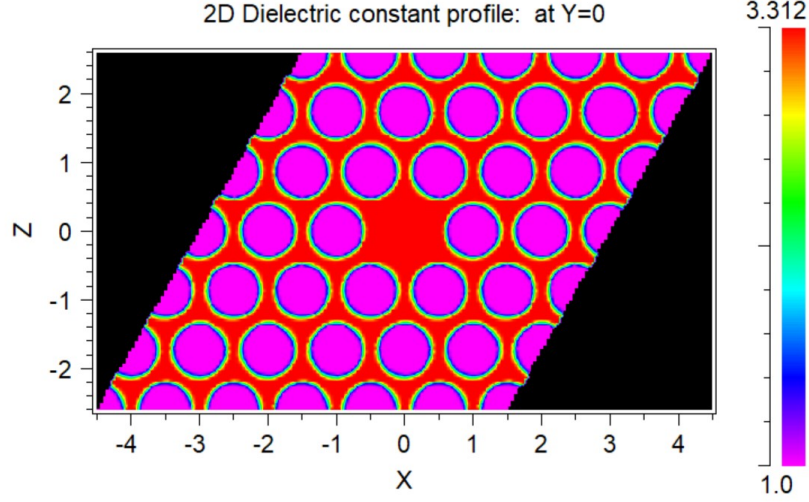


**Figure 3.15:** First periodic domain of integration considered. The legend indicates the colour coding used for the electrical permittivity

The first calculation to be made is putting in MOST a constant value of the wave vector  $\mathbf{K} = (0, 10, 0)[\mu m^{-1}]$ , i.e., 628 nm wavelength. The values obtained will be the effective index and the frequency for the first 8 modes. These values are presented in the table 3.3, as the waveguide defect is an area of high refractive index, it will be possible to detect the propagation modes with the first modes presented. This is possible since the effective index can be expressed as  $n_{eff} = k/w$ , and as the first modes are the lowest frequency modes, these will correspond to the highest effective indices. That is to say, those that are on average more confined in the high index defect.

Modes	$n_{ef}$	frequency ( $wa/2\pi c = a/\lambda$ )
0	1.7322	0.918782
1	1.7322	0.918788
2	1.6307	0.976007
3	1.6209	0.981908
4	1.6206	0.982083
5	1.6206	0.982102
6	1.5385	1.03451
7	1.5329	1.03825

**Table 3.3:** Frequencies and effective indices values of the first 8 modes for Bloch wave vector  $\mathbf{K} = (0, 10, 0)[\mu m^{-1}]$

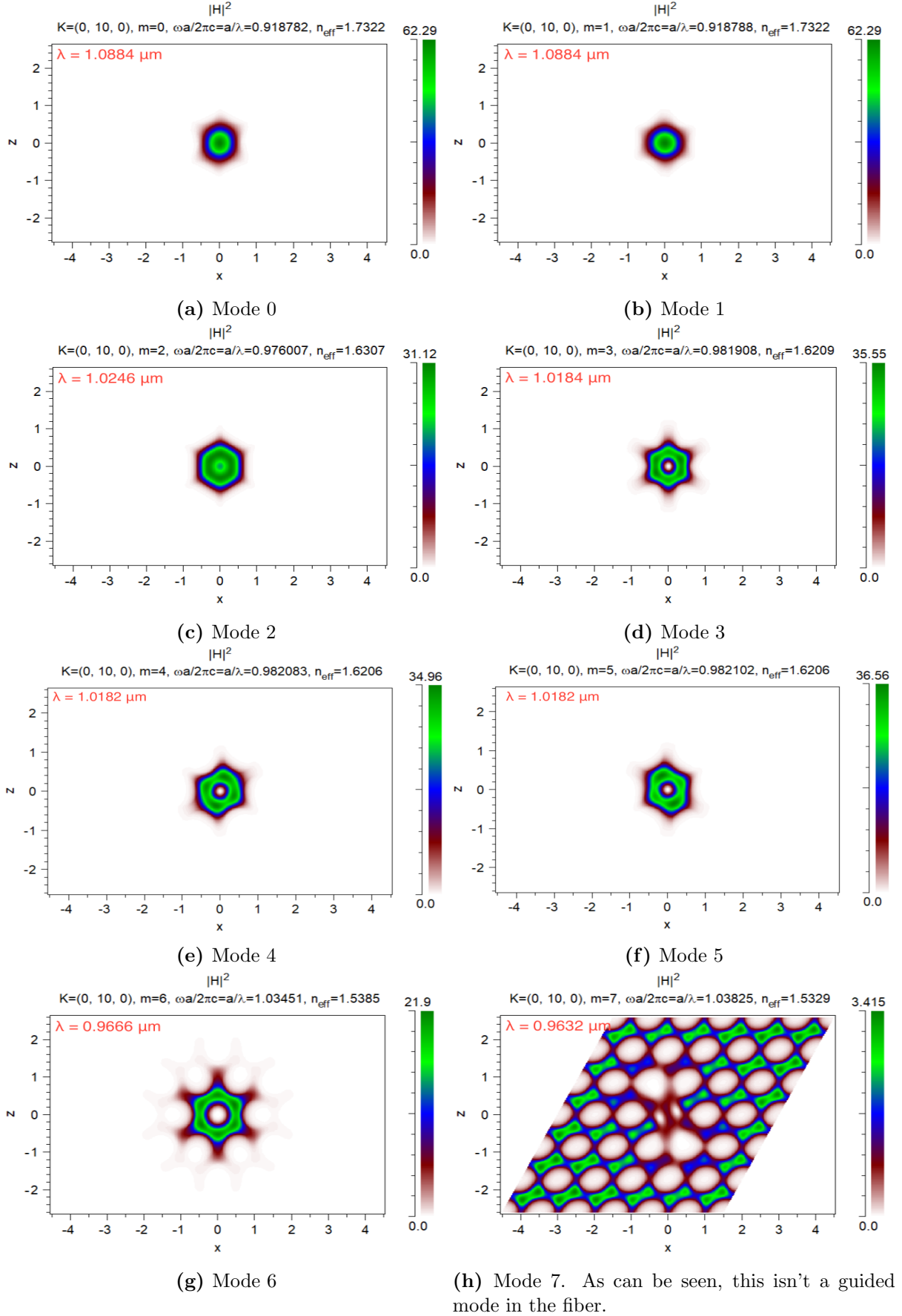


**Figure 3.16:** Spatial distribution of the squared magnetic intensity for each mode. Axis units in microns and free-space wavelength indicated in red.

Figure 3.16 shows the squared magnetic fields of the first seven solutions of the propagation of light for the above-mentioned wave vector  $\mathbf{K}$ . Modes 0 and 1 appear to be degenerate modes of the fundamental mode, where both carry light through the centre of the defect but with orthogonal polarisation. The following modes are higher order modes, also bonded to the defect, where modes 4 and 5 also appear to be degenerate modes with orthogonal polarisations. However, mode 7 is clearly the beginning of pure radiative modes, modes where the light does not travel concentrated through the core of the wave guide.

## Second integration domain

Shown in figure 3.17, it is considered now the domain corresponding to a square. Compared to figure 3.15, the spatial range on the z-axis is the same as that considered previously and on the x-axis it is larger and with a number of pores equivalent to those along the z-axis. This will allow a greater separation of the defect repetition in the x-axis and therefore a greater similarity in the calculation to the desired waveguide with only one defect in the centre.

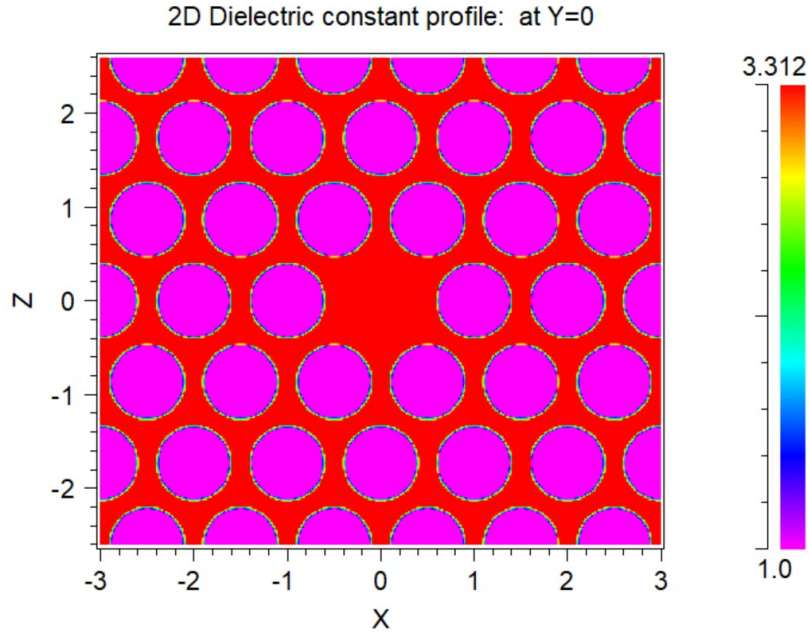


**Figure 3.17:** Second integration domain considered.

The effective index and frequency calculations for the first eight modes with previous  $\mathbf{K}$  wave vector are performed again. The results are shown in the table 3.4.

Modes	$n_{ef}$	frequency ( $wa/2\pi c = a/\lambda$ )
0	1.7322	0.918776
1	1.7322	0.918778
2	1.6307	0.975988
3	1.6209	0.981879
4	1.6206	0.982071
5	1.6206	0.982075
6	1.5385	1.03445
7	1.5330	1.03816

**Table 3.4:** Frequencies and efective indices for the first eight modes considering second domain of integration.

Comparing the results between tables 3.3 and 3.4, it can be seen how the frequency values for the set of modes  $[0,1]$  and  $[4,5]$  were very close in table 3.3 and even closer in table 3.4. Verifying that these pairs of modes are degenerate solutions, as it was discussed with figure 3.16. On the other hand, there are no substantial differences in the distribution of the squared magnetic fields for these modes using the new integration domain.

In order to also characterise the waveguide, MOST is used again to obtain the effective indices and frequencies of the first 6 modes, but for a range of vector  $\mathbf{K}$  from  $(0, 1, 0)$  to  $(0, 30, 0)$   $[\mu m^{-1}]$ . Results are presented in figure 3.18.

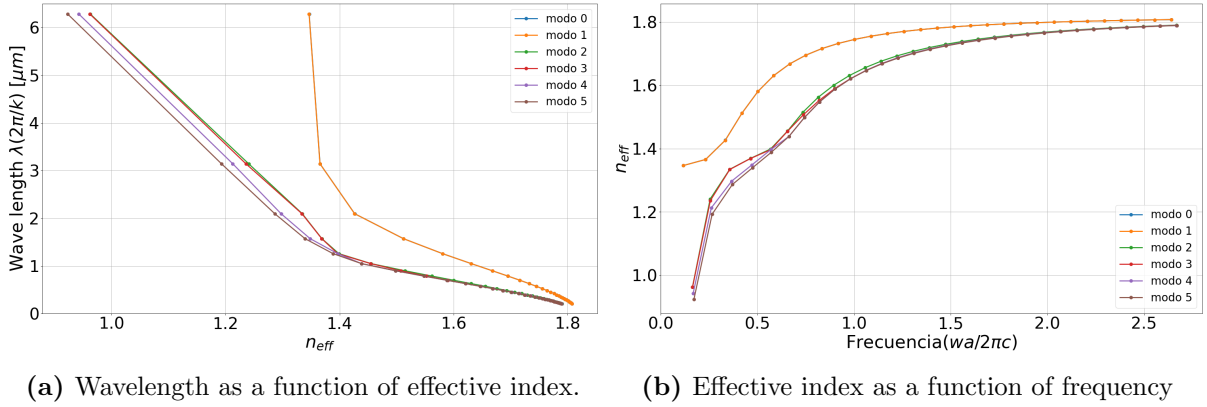


**Figure 3.18:** Modes traversing the vector  $\mathbf{K}$  in longitudinal direction from  $(0, 1, 0)$  to  $(0, 30, 0)$   $[\mu m^{-1}]$ .

The two figures tell something similar. As can be seen, as the wavelength decreases (or the frequency increases) the effective index of all modes increases, therefore these modes are in general<sup>4</sup> more confined in the guide. On the other hand, for longer wavelengths,

<sup>4</sup>To be sure, it MUST be necessary to see the squared magnetic fields plots of these modes. However, this can serve as a first approach.

the confinement decreases with a worse tendency for modes 2 to 5 than for the two fundamental modes 0 and 1, giving the possibility of having a single-mode guide. Even for modes 0 and 1, overlapped in the plots as they are degenerate, it is possible that they are also radiative modes for a wavelength of 6 microns, as the effective index drops to 1.38. In addition, it is interesting to note how modes 4 and 5, classified as degenerate for  $K=(0,10,0)$ , decouple and become radiative for long wavelengths.

The next step is to calculate the V number, which is an indicator of whether or not there is a single mode of propagation within the waveguide. If the value to which the V-number tends as  $k_y$  increases is greater than 2.405, then the waveguide is not single-mode. Otherwise, the waveguide is single-mode. The V-number is defined as:

$$V_{eff} = 2\pi \frac{\Delta}{\lambda} \sqrt{n_o^2 - n_{eff}^2} \quad (3.2)$$

where  $n_{eff}$  will correspond to the effective refractive index of the first mode of the lattice without the defect in the centre.

Therefore, since what is of interest is the value to which the V number tends, to better sample with MOST, the wave vector  $\mathbf{K}$  is traversed from  $(0, 0.1, 0)$  to  $(0, 70, 0)$  [ $\mu m^{-1}$ ] logarithmically. From the program calculations, the values of the frequency and the effective index for the first mode of the lattice without defect will be obtained. With this data, the equation 3.2 can then be applied to obtain the values of the V-number. The results are shown in figure 3.19.

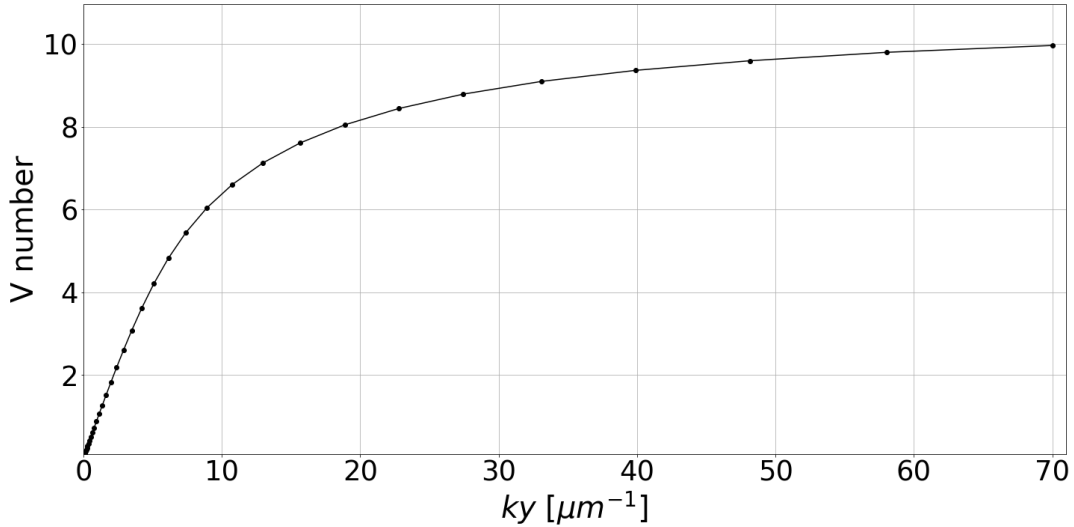


**Figure 3.19:** V number as a function of  $k_y$ .

In figure 3.19 it can be seen how the value of the V number tends to 10, much higher than the value of 2,405. This result indicates that the waveguide is not single-mode, which was to be expected from all discussed.

### 3.3.4 Fabrication of an hexagonal lattice

In order to test whether these structures can be fabricated using the 3DLW technique with our femtosecond laser setup, a hexagonal lattice of nanopores was constructed by

wet-chemical etching the lithographed zones. The lattice obtained has a lattice parameter of 250 nm and nanopores with mean widths of  $109 \text{ nm} \pm 8 \text{ nm}$ , and heights of  $125 \text{ nm} \pm 10 \text{ nm}$ . Therefore, it has an ellipticity of  $1.14 \pm 0.18$ , so the pores have a very circular shape. Using equation 2.7 and error propagation theory (error equation in appendix B), the FF of this lattice is  $0.20 \pm 0.03$ .

As can be seen in figure 3.20, the lattice was made correctly in the inner zones. However, due to the polishing process, pore overlapping has occurred at the edges, as it is where the stress of the pore structure is concentrated. At least, this phenomenon only occurs in the surface layer and the pore structures are still intact behind. Therefore, in order to reduce this effect, a finer polishing process should be carried out.

Also, recovering figure 3.11 and in order to obtain the lattice with the largest TM band gap, for PCF applications for example, it would be necessary to leave the sample etching more time to increase the pore diameter to approaches the optimum. As for all the spectral ranges studied, the larger TM band gap with  $1 \mu\text{m}$  lattice parameter is around  $0.8 \mu\text{m}$ , this corresponds to leave etching our sample until 0.58 FF.

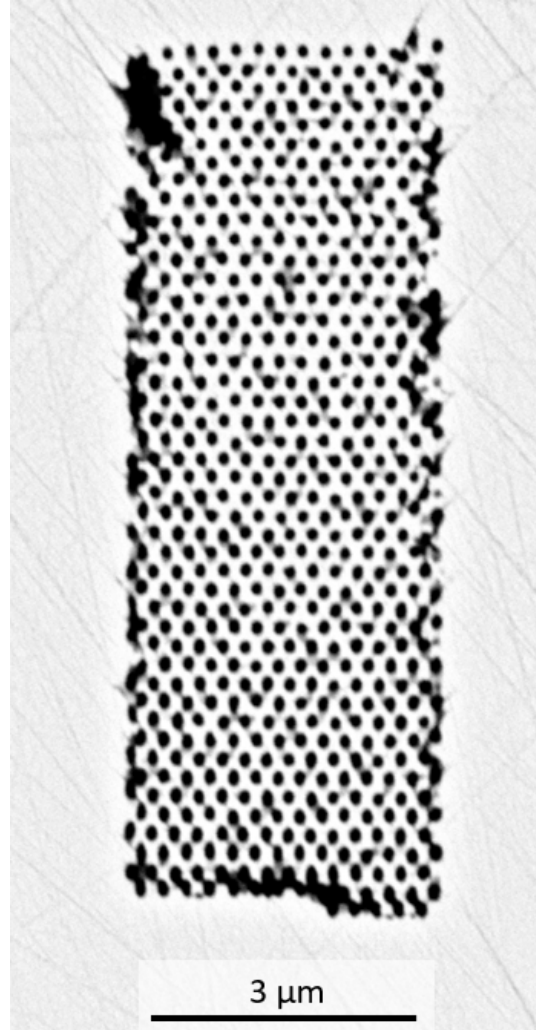


**Figure 3.20:** Hexagonal lattice made by 3D laser writing. FF is  $0.20 \pm 0.03$  and lattice parameter 250 nm.

## 4. Conclusions

---

### *Resumen*

---

En este apartado se presentan las principales conclusiones que se pueden extraer del trabajo desarrollado. En primer lugar, en el ámbito experimental, se identifican configuraciones láser que logran un mayor ritmo de grabado químico en YAG, se establece una dependencia de la energía del pulso láser utilizado con la forma transversal de los nanopores de aire obtenidos, y se concluye el orden de magnitud del cambio de índice de refracción en YAG debido a 3DLW y las implicaciones que tiene. En segundo lugar, respecto a las simulaciones numéricas, se ha podido identificar los diámetros de poros con un *bandgap* fotónico mayor y los modos confinados para una guía de onda microestructurada. Esto último hace posible, que para ciertas frecuencias, se pudiera observar un comportamiento mono-modo. Además, se presentan líneas futuras trabajo como el uso de otros cristales ópticos y se concluye el potencial que tiene esta técnica para el desarrollo de estructuras fotónicas en el futuro.

---

From the results obtained in the experimental field, it can be concluded the dependence of the writing speed, together with other laser parameters used in 3D laser writing, on the etching rate of the nanopores in YAG optical crystal. Although it has not been possible to characterise the optimum writing speed for certain laser setups, in the case of 1 MHz repetition frequency and 17nJ energy pulse, the writing speed at which the lithography zone is etched the fastest can be concluded to be  $\sim 0.45$  mm/s. In addition, from the results of the transverse pore size, it has been found that, as the laser pulse energy decreases, the pore diameters obtained become smaller and smaller and with less ellipticity. In this way, pores with an ellipticity of  $1.41 \pm 0.29$  and pore widths of less than a hundred nanometres have been achieved. On the other hand, thanks to the Wave Front Phase Imaging (WFPI) technique, it has been possible for the first time to obtain that the change in refractive index of YAG due to laser lithography is of the order of  $10^{-2}$ . This refractive index change value could enable the creation of step index fibers (SIFs) as possible light-guiding method. Finally in the experimental part, a hexagonal lattice of nanopores has been successfully fabricated with a Filling Factor of  $0.20 \pm 0.03$ , a lattice parameter of 250 nm and a really low pore ellipticities of  $1.14 \pm 0.18$ , which allows to verify the possibilities of this technique for the fabrication of photonic structures.

Regarding the computational simulations, the study was done for a hexagonal lattice of air nanopores within YAG crystal, also considering  $1 \mu\text{m}$  as lattice parameter. From the results obtained, it can be concluded that the optimum bandgap is found to be for the light propagating with its electric field within the cross-sectional plane. In this way, the pore diameter for which the TM bandgap is the largest is located between 0.75-0.8 microns and with a dimensionless frequency bandgap width of 0.053-0.085, depending on the spectral range. This photonic bandgap found is really interesting for light-guiding purpose, as it can be applied for a development of a Photonic Crystal Fiber (PCF). On the other hand, for the waveguide created with the hexagonal lattice cladding and a

pore defect as core, up to 7 modes confined within the fiber core are found, using a bloch vector in the longitudinal direction equal to  $10 \text{ } (\mu\text{m}^{-1})$ . In addition, the loss of confined modes for lower K vectors, and a greater confinement of these propagation modes for higher K vectors, is concluded. The possibility of achieving a single-mode waveguide for a given value of K is also considered, which is useful for long-range guides.

As future lines of work, it would be interesting to carry out this study for other optical crystals that have also been observed to have high etching rates in 3DLW zone, such as sapphire, in order to check if the results are better. In addition, the lack of knowledge of the exact chemical reaction that takes place in wet-etching allows to investigate other types of acidic solutions that could have higher etching rates. Regarding the bandgaps, other types of cladding with more elaborated crystalline structures could be tested to see if the bandgaps obtained are better than the one studied in this work. In conclusion, the excellent results obtained in this study allow us to focus on this 3DLW plus wet-etching technique for the development and implementation of photonic structures in the technology sector.



## 5. References

---

- [1] Dunzhao Wei, Chaowei Wang, Xiaoyi Xu, Huijun Wang, Yanlei Hu, Pengcheng Chen, Jiawen Li, Yunzhi Zhu, Chen Xin, Xiaopeng Hu, et al. Efficient nonlinear beam shaping in three-dimensional lithium niobate nonlinear photonic crystals. *Nature communications*, 10(1):1–7, 2019.
- [2] Shining Zhu. Meter-level optical delay line on a low-loss lithium niobate nanophotonics chip. *Chinese Physics Letters*, 37(8):080102, 2020. doi: 10.1088/0256-307X/37/8/080102.
- [3] J. del Hoyo, R. Martínez Vázquez, B. Sotillo, Toney Teddy Fernandez, Jan Siegel, Paloma Fernández, R. Osellame, and Javier Solís Céspedes. Control of waveguide properties by tuning femtosecond laser induced compositional changes. *Applied Physics Letters*, 2014. doi: 10.1063/1.4896846.
- [4] Jinman Lv, Binbin Hong, Yang Tan, Feng Chen, Javier Rodríguez Vázquez de Aldana, and Guo Ping Wang. Mid-infrared waveguiding in three-dimensional microstructured optical waveguides fabricated by femtosecond-laser writing and phosphoric acid etching. *Photon. Res.*, 8(3):257–262, Mar 2020. doi: 10.1364/PRJ.380215.
- [5] C Wochnowski, S Metev, and G Sepold. Uv–laser-assisted modification of the optical properties of polymethylmethacrylate. *Applied Surface Science*, 154-155:706–711, 2000. ISSN 0169-4332. doi: [https://doi.org/10.1016/S0169-4332\(99\)00435-3](https://doi.org/10.1016/S0169-4332(99)00435-3).
- [6] LV Keldysh et al. Ionization in the field of a strong electromagnetic wave. *Sov. Phys. JETP*, 20(5):1307–1314, 1965.
- [7] Shoji Maruo, Osamu Nakamura, and Satoshi Kawata. Three-dimensional microfabrication with two-photon-absorbed photopolymerization. *Opt. Lett.*, 22(2):132–134, Jan 1997. doi: 10.1364/OL.22.000132.
- [8] Jerome Lapointe, Jean-Philippe Bérubé, Yannick Ledemi, Albert Dupont, Vincent Fortin, Younes Messaddeq, and Réal Vallée. Nonlinear increase, invisibility, and sign inversion of a localized fs-laser-induced refractive index change in crystals and glasses. *Light: Science & Applications*, 9(1):1–12, 2020.
- [9] Airán Ródenas, Min Gu, Giacomo Corrielli, Petra Paiè, Sajeev John, Ajoy K. Kar, and Roberto Osellame. Three-dimensional femtosecond laser nanolithography of crystals. *Nature photonics*, (2), 2019. doi: 10.1038/s41566-018-0327-9.
- [10] Spectra-Physics. Millennia® eV™ High Power CW DPSS Lasers. 2021. <https://www.spectra-physics.com/en/f/millennia-ev-cw-dpss-laser>.
- [11] Spectra-Physics. Tsunami® Ultrafast Ti:Sapphire Oscillators. 2021. <https://www.spectra-physics.com/en/f/tsunami-ultrafast-oscillator>.

- [12] Alfredo Casasnovas Melián and Airán Ródenas Seguí. Design of sub-wavelength transmission gratings fabricated by means of 3d femtosecond nanolithography, TFM. 2021.
- [13] Sergio Catalán Torralbo and Airán Ródenas Seguí. Microplastic analysis in sea urchins *Diadema africanum* via Raman Spectroscopy, TFG. 2021.
- [14] Thermo Fisher. Electrons in SEM. 2022. <https://www.thermofisher.com/es/es/home/materials-science/learning-center/applications/sem-electrons.html#:~:text=Backscattered%20vs%20secondary%20electrons&text=Backscattered%20electrons%20are%20reflected%20back,electron%20beam%20and%20the%20sample.>
- [15] Juan M Trujillo-Sevilla, Miriam Velasco-Ocaña, Sergio Bonaque-González, Carolina Belda-Para, and José M Rodríguez-Ramos. Wavefront phase measurement of striae in optical glass. *Applied Optics*, 61(14):3912–3918, 2022.
- [16] S Bonaque-González, JM Trujillo-Sevilla, Ó Velasco-Ocaña, M Casanova-González, M Sicilia-Cabrera, A Roqué-Velasco, S Ceruso, R Oliva-García, J Martín-Hernández, O Gomez-Cardenes, JG Marichal-Hernández, D Gatinel, JT Holladay, and JM Rodríguez-Ramos. The optics of the human eye at 8.6  $\mu\text{m}$  resolution. *Sci Rep*, 12 2021.
- [17] J. Hrabovský, M. Kučera, L. Paloušová, L. Bi, and M. Veis. Optical characterization of Y3Al5O12 and Lu3Al5O12 single crystals. *Opt. Mater. Express*, 11(4):1218–1223, Apr 2021. doi: 10.1364/OME.417670.
- [18] Trifon Todorov Trifonov. Photonic bandgap analysis and fabrication of macroporous silicon by electrochemical etching. Doctoral thesis. *Universitat Rovira i Virgili*, 2004.
- [19] Dr. Raymond C. Rumpf. Lecture 4c: Unit cells & brillouin zone. In *21st Century Electromagnetics*. 2021.
- [20] Dr. M. Pilar Aceituno Cantero. Estructura Cristalina 2: Red Recíproca. In *Física del Estado Sólido, Grado en Física*. 2020.
- [21] Inc. Synopsys. RSoft BandSOLVE User Guide. 2019.
- [22] Dr. Raymond C. Rumpf. Lecture 4d: Electromagnetic waves in periodic structures. In *21st Century Electromagnetics*. 2021.
- [23] John R. Taylor. Introduction to error analysis, the study of uncertainties in physical measurements, 2nd edition. 1997.
- [24] Airán Ródenas and Ajoy Kar. High-contrast step-index waveguides in borate nonlinear laser crystals by 3d laser writing. *Optics express*, 19:17820–33, 08 2011. doi: 10.1364/OE.19.017820.

# Appendix

## A. Cross-sectional pore measurements

---

	Area( $nm^2$ )	Perim.( $nm$ )	Major( $nm$ )	Minor( $nm$ )
1	423000	3090	1181	456
2	432000	3090	1200	459
3	434000	3100	1192	464
4	426000	3060	1213	448
5	444000	3160	1217	465
6	444000	3120	1220	464
7	434000	3060	1209	458
8	442000	3120	1212	465
9	438000	3060	1200	465
10	442000	3190	1212	465
11	452000	3100	1201	480
12	446000	3190	1218	467
13	438000	3120	1202	464
14	444000	3200	1208	468
15	442000	3120	1215	464
16	446000	3100	1188	478
17	385000	2880	1128	434
18	419000	2970	1149	464
19	426000	3030	1178	461
20	415000	3000	1137	464
21	122000	1690	628	247
22	120000	1660	631	243
23	125000	1740	646	246
24	119000	1570	619	244
25	86000	1360	498	219
26	93000	1380	529	223
27	87000	1420	525	211
28	90000	1400	531	215
29	43000	860	332	166
30	45000	960	339	169
31	38000	870	311	157
32	46000	970	350	168

**Table A.1:** All cross-sectional measurements of pores. Pulse energy decreases every four measurements

## B. Error propagation

---

If  $n$  variables  $x_0, x_1, \dots, x_n$  are directly measured with an error  $\delta x_0, \delta x_1, \dots, \delta x_n$ , the error of a function  $f(x_0, x_1, \dots, x_n)$  is approximated with a Taylor series up to first order<sup>23</sup>:

$$\delta f(x_0, x_1, \dots, x_n) = \sum_{i=0}^n \frac{\partial f(x_0, x_1, \dots, x_n)}{\partial x_i} \cdot |\delta x_i|$$

Resulting error propagation formula with this method:

- Ellipticity  $e$  of the cross-plane of pores with major axis  $a$  and minor axis  $b$ :

$$e = a/b$$

Applying logarithms:

$$\ln(e) = \ln(a)/\ln(b)$$

Doing now error propagation:

$$\delta e = e \left( \frac{\delta a}{a} + \frac{\delta b}{b} \right)$$

- OPD respected to 3DLW zone:

$$OPD_{3DLW}(y) = OPD(x = 67, y) - OPD(x = 54, y)$$

Thus, the error is:

$$|\delta OPD_{3DLW}| = |\delta OPD| + |\delta OPD|$$

where  $\delta OPD$  is equal to 5nm and corresponds to the instrumental error of WFPI instrument, the same for all XY points in the OPD map (figure 3.7). For averages along Y-axes the error is the same.

- Refractive index change in 3DLW zone using averaged OPD on Y-axis (equation 2.3):

$$\Delta n = \frac{\overline{OPD}_{x=67} - \overline{OPD}_{x=54}}{\Delta z}$$

Applying logarithms:

$$\ln(\Delta n) = \ln(\overline{OPD}_{x=67} - \overline{OPD}_{x=54}) - \ln(\Delta z)$$

Now, the function for error propagation,  $f$ , is  $\ln(\Delta n)$ :

$$\delta \ln(\Delta n) = \frac{|\delta \overline{OPD}| + |\delta \overline{OPD}|}{\overline{OPD}_{x=67} - \overline{OPD}_{x=54}} + \frac{|\delta \Delta z|}{\Delta z}$$

Aproximating  $\delta \ln(\Delta n)$  as a derivative and operating it is obtained the final formula:

$$\delta \Delta n = \Delta n \left( \frac{2|\delta \overline{OPD}|}{\overline{OPD}_{x=67} - \overline{OPD}_{x=54}} + \frac{|\delta \Delta z|}{\Delta z} \right)$$

- Filling factor (FF) in terms of diameter:

$$FF = \frac{A_{pr}}{A_r} = \frac{2\pi}{4\sqrt{3}} \left( \frac{d}{a} \right)^2$$

Doing error propagation:

$$\delta FF = \frac{\pi d}{\sqrt{3} a^2} \delta d$$